

Geochemistry, Geophysics, Geosystems



RESEARCH ARTICLE

10.1029/2021GC009927

Global Induced Stress Field From Large Earthquakes Since 1900 and Chained Earthquake Occurrence

Junhyung Lee¹  and Tae-Kyung Hong¹ 

¹Department of Earth System Sciences, Yonsei University, Seoul, South Korea

Key Points:

- The stress fields in subduction zones were highly perturbed by precedent large earthquakes
- Descendant large earthquakes dominantly occur in the regions of high stress contrasts
- The stress perturbation by precedent earthquakes may be a major factor controlling global seismicity

Supporting Information:

Supporting Information may be found in the online version of this article.

Correspondence to:

T.-K. Hong,
tkhong@yonsei.ac.kr

Citation:

Lee, J., & Hong, T.-K. (2021). Global induced stress field from large earthquakes since 1900 and chained earthquake occurrence. *Geochemistry, Geophysics, Geosystems*, 22, e2021GC009927. <https://doi.org/10.1029/2021GC009927>

Received 17 DEC 2020

Accepted 26 JUL 2021

Abstract Megathrust earthquake occurrence is dependent on the physical properties and stress environments of convergent plate boundaries. Local and regional earthquakes may modulate the stress environment fractionally that affects the nucleation of next earthquakes. This study investigates the influence of precedent earthquakes on the induction of forthcoming earthquakes around the circum-Pacific plate boundaries. We assess the global stress perturbation induced by 1,636 earthquakes combining 1,457 earthquakes with moment magnitudes greater than or equal to M_w 7.0 and 179 earthquakes with moment magnitudes M_w 6.4–6.9 in 1900–2020. We stack the induced Coulomb stress changes for optimally oriented reverse faults. The circum-Pacific region is divided by eight subregions. The cumulative Coulomb stress changes reach up to the order of tens to hundreds of bar at the convergent plate boundaries. Descendant large earthquakes dominantly occurred in the regions with large lateral gradients of cumulative Coulomb stress changes induced by precedent earthquakes. The cumulative Coulomb stress changes for 120 years are comparable among subduction zones. The seismicity in subduction zones may depend on the strength of the stress field as well as the lateral gradient in the stress field. The instability and inhomogeneity in stress fields may play a major role in the nucleation of megathrust earthquakes.

Plain Language Summary Great earthquakes produce significant damages over large areas. The timely identification of impending earthquakes is crucial for seismic hazard mitigation. We assess the stress induced from neighboring earthquakes for 120 years around the circum-Pacific plate boundaries. Large earthquakes perturbed the stress fields. We analyze 1,636 earthquakes with moment magnitudes greater than or equal to 6.4 in 1900–2020. The cumulative Coulomb stress changes reach up to the order of tens to hundreds of bar at the plate boundaries. Large earthquakes followed in the regions with large lateral gradients of cumulative Coulomb stress changes induced by precedent earthquakes. Laterally heterogeneous stress fields may play an important role in nucleation of great earthquakes.

1. Introduction

Most great earthquakes occurred in the circum-Pacific seismic zone, producing large seismic damages (Obara & Kato, 2016; R. E. Wells & Blakely, 2003; Ye et al., 2018). The prediction of impending great earthquakes may be important for timely mitigation of seismic hazards. Tectonic loading may be a principal force to nucleate earthquakes (Gardi et al., 2006; Ide, 2013; Qiu & Shi, 2004; Uyeda & Kanamori, 1979). In particular, the spatial distribution of strain accumulation during the interseismic period may control large earthquake occurrence (Konca et al., 2008; Liberty et al., 2013). The interplate coupling may be inferred from slip deficit and strain rate (Yokota et al., 2016). Additionally, slab geometry, asperity, slow slip, thermal environment, stable sliding, and fluid contents may play additional roles in nucleation of earthquakes on plate boundaries (Araki et al., 2017; Chapman & Melbourne, 2009; Hippchen & Hyndman, 2008; Keiding et al., 2009; Perfettini & Avouac, 2004; Saffer et al., 2000; Schwartz & Rokosky, 2007; Townend & Zoback, 2006; Uchida et al., 2016; R. E. Wells & Blakely, 2003; Yokota et al., 2016).

It was recognized that oceanic sediment is a major resource of fluids delivered on the slab surface (Ruff, 1989; Seno, 2017). Recently, it was suggested that sediment density may be more important than sediment thickness (Han et al., 2017). The overpressurized fluids from slab sediments or hydrated minerals may compose environments which are favorable to accommodate great earthquakes along interplate boundaries (Delouis et al., 1996; Hasegawa, 2017; Saffer et al., 2000; Streit & Cox, 2001). However, it is difficult to measure the induced pore fluid pressures and fault strengths on the interplate boundaries.

© 2021. The Authors.

This is an open access article under the terms of the [Creative Commons Attribution-NonCommercial-NoDerivs License](https://creativecommons.org/licenses/by-nc-nd/4.0/), which permits use and distribution in any medium, provided the original work is properly cited, the use is non-commercial and no modifications or adaptations are made.

Efforts were devoted to study the stress loading procedure and mechanism (Araki et al., 2017; Dixon et al., 2014; Obara & Kato, 2016; Uchida et al., 2016; Yokota et al., 2016). Slip deficits may reflect the stresses accumulated on slab surfaces (Yokota et al., 2016). The stress on a slab surface may be further modulated by slow earthquakes. However, the physical mechanism and relationship between stress accumulation and release by slow slips were only minimally understood (Araki et al., 2017; Obara & Kato, 2016; Saffer & Wallace, 2015; Uchida et al., 2016; Wallace et al., 2016).

There were manifold observations on the nature of megathrust earthquake nucleation environments. Suggestions included the asperity of the strong crust of upper plates (Beck & Christensen, 1991; Ryan & Scholl, 1993), subducting seamounts (Cloos, 1992; Cloos & Shreve, 1994), or apparent presentations of seismic gaps (Scholz, 1990; Thatcher, 1990). A megathrust earthquake may occur by rupturing a part of one asperity or several asperities successively (Konca et al., 2008; Rundle & Kanamori, 1987). Additionally, rigorous efforts were devoted to understanding the relative influence of each factor on the megathrust earthquake nucleation (Oleskevich et al., 1999).

The triggering mechanisms of megathrust earthquakes have, however, been only poorly understood. Stress transferred from adjacent earthquakes often affects the seismicity (McCloskey et al., 2005; Stein et al., 1997; Toda et al., 2012). In particular, stress shadows may last for tens to hundreds of years, thus preventing the occurrence of subsequent earthquakes (Liu et al., 2018; Maccafferri et al., 2013; Sevilgen et al., 2012). It was suggested that stress transfer plays a role in earthquake nucleation (Boyd et al., 1999; Schwartz, 1999). The transferred stress is crucial in temporal seismicity evolution (Bowman & King, 2001; Nalbant et al., 1998).

The earthquake magnitude–frequency relationship, maximum magnitude, and yield stress level may differ according to the subduction zone depending on the slab geometry, thermal environment, and fluid contents (Currie et al., 2002; Hicks et al., 2012; Hippchen & Hyndman, 2008; Koerner et al., 2004). There were 19 great earthquakes with moment magnitudes greater than or equal to 8.5 in 1900–2020. However, the earthquakes were distributed unevenly over time, presenting temporal clustering. Six recent great earthquakes occurred from 2004 to 2012. The temporal clustering of great earthquakes suggests that temporal factors may play a crucial role in nucleation. Thus, temporal evolution of influencing factors is important.

Large earthquakes may induce significant dynamic and static stress changes, triggering earthquakes at local and regional distances (King & Cocco, 2001; Stein et al., 1997; Toda et al., 2012). The postseismic earthquakes with moment magnitudes of 4.0–5.0 are generally correlated with the Coulomb stress changes induced by precedent earthquakes (Ammon et al., 2008; Cocco et al., 2000; Stein et al., 1997). The aftershock rate and size are dependent on the level of induced stress (Felzer et al., 2004; Harris & Simpson, 1998; King et al., 1994; J. Lin & Stein, 2004; Ma et al., 2005; Nalbant et al., 1998; Stein et al., 1994, 1997; Toda et al., 2005). There are, however, some controversial reports regarding the influence of stress shadows on postseismicity (Green et al., 2015; Hong et al., 2015; W.-H. Wang, 2000).

We investigate the temporal changes in the stress field for 120 years and the correlation with postseismicity of moderate-size earthquakes in the circum-Pacific seismic zone, which is the most active seismic zone (Figure 1a). The influence of the precedent earthquakes is examined by comparison between the cumulative Coulomb stress changes and descendant seismicity. We consider only the induced stress from neighboring and precedent earthquakes. We assess the total amount of induced stress. We infer the influence of induced stress on the triggering of great earthquakes. This approach may allow us to quantify the variance of stress with time along plate boundaries. We may quantify the occurrences of stress field changes.

2. Data

We collect the event information of global earthquakes since 1900 (Ammon et al., 2005; Asano et al., 2005; Baba et al., 2002; Courboux et al., 1997; Elliott et al., 2010; Engdahl & Villaseñor, 2002; Fujii & Satake, 2013; Fukuyama & Irikura, 1986; Hartzell & Langer, 1993; Hayes, 2017; Hernandez et al., 2001; Ichinose et al., 2002, 2003; Ji et al., 2002; Johnson & Satake, 1999; Kobayashi & Koketsu, 2005; Lay et al., 2005; Mai & Thingbaijam, 2014; Mendoza, 1993, 1995; Mendoza & Hartzell, 1989, 2013; Mendoza et al., 1994; Moreno et al., 2010; Nagai et al., 2001; Okuwaki & Yagi, 2002; Ozawa et al., 2011; Ross et al., 2019; Sekiguchi et al., 2002; Song et al., 2008; Wald & Heaton, 1994; Yagi, 2004; Yagi et al., 1998; Yamanaka & Kikuchi, 2004;

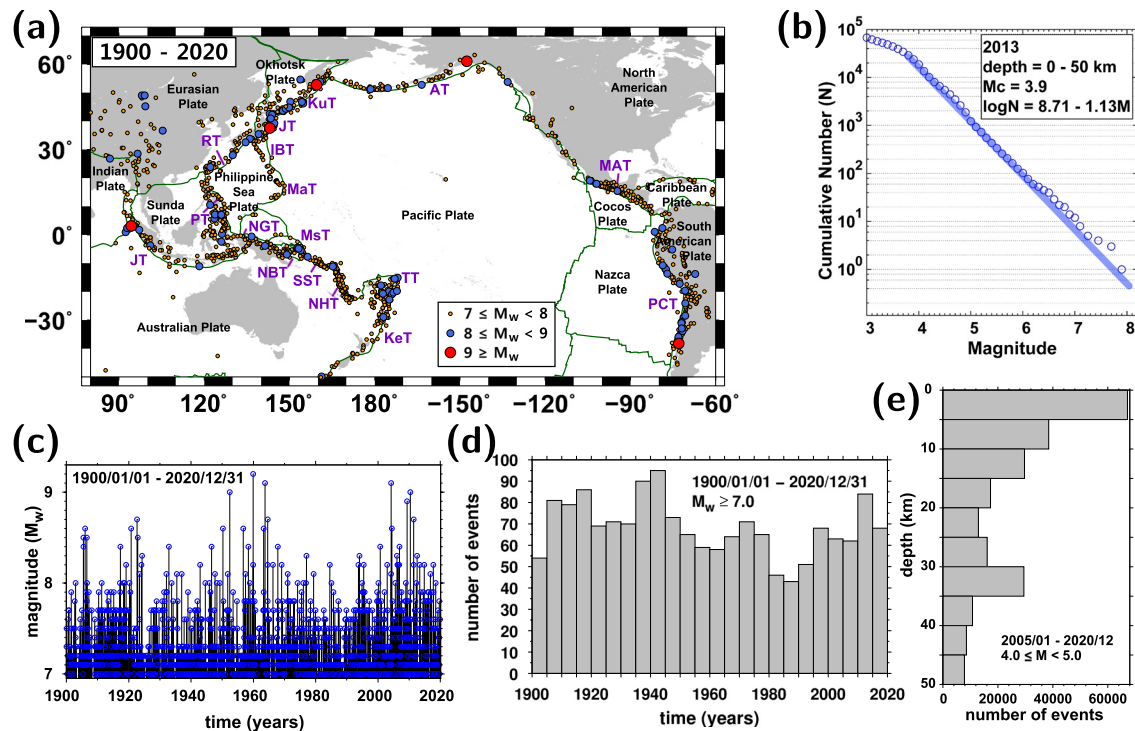


Figure 1. Global seismicity and zonation. (a) Earthquakes with moment magnitudes greater than or equal to 7.0 during 1900–2020. The large earthquakes are distributed uniformly along the plate boundaries. Major subduction zones are indicated: Aleutian Trench (AT), Izu-Bonin Trench (IBT), Japan Trench (JT), Java Trench (JT), Kermadec Trench (KeT), Kuril Trench (KuT), Manus Trench (MsT), Mariana Trench (MaT), Middle America Trench (MAT), New Britain Trench (NBT), New Guinea Trench (NGT), New Hebrides Trench (NHT), Peru-Chile Trench (PCT), Philippine Trench (PT), Ryukyu Trench (RT), South Solomon Trench (SST), Tonga Trench (TT). (b) Gutenberg-Richter frequency-magnitude relationship of global seismicity with focal depths of 0–50 km in 2013. The minimum magnitude ensuring the completeness of the earthquake catalog is 3.9. The b value is 1.13. (c) Temporal distribution of earthquakes with moment magnitudes greater than or equal to 7.0 since 1900. (d) Temporal variation in the numbers of large earthquakes. (e) Focal depths of earthquakes with moment magnitudes of $4.0 \leq M_w < 5.0$ from 2005 to 2020.

Ye et al., 2013). We additionally collect the event information for earthquakes since 2005 from the International Seismological Centre (www.isc.ac.uk). There are 1,457 earthquakes with moment magnitudes greater than or equal to 7.0 in 1900–2020 (Figure 1a). We additionally find 179 earthquakes with moment magnitudes M_w 6.4–6.9 in 1900–2020 to compensate the low seismicity region. We, thus, analyze 1,636 earthquakes with magnitudes $\geq M_w$ 6.4 in 1900–2020 (Supporting Information S1).

The minimum moment magnitude of earthquakes, certifying the completeness of the earthquake catalog, is 3.9 (Figure 1b). The largest moment magnitude is M_w 9.5 (Figure 1c). The numbers of earthquakes with magnitudes $M_w \geq 7.0$ for every 5 years since 1900 range between 43 and 95 (Figure 1d). Moderate earthquakes of M_w 4.0–5.0 are populated at depths less than 35 km (Figure 1e). We additionally collect the information of historical earthquakes to complement the instrumental seismicity records (Albini, Musson, Gomez Capera, et al., 2014; Albini, Musson, Rovida, et al., 2014; Beck et al., 1998).

We divide the plate boundaries around the circum-Pacific seismic zone into eight subregions (Figure 2a). We collect the source parameters (event magnitudes, fault lengths, fault widths, slip amounts) and focal mechanism solutions of large earthquakes in 1900–2020 from Global Centroid Moment Tensor (CMT) catalog (www.globalcmt.org) as well as available resources (Ammon et al., 2005; Asano et al., 2005; Baba et al., 2002; Courboux et al., 1997; Elliott et al., 2010; Engdahl & Villaseñor, 2002; Fujii & Satake, 2013; Fukuyama & Irikura, 1986; Hartzell & Langer, 1993; Hayes, 2017; Hernandez et al., 2001; Ichinose et al., 2002, 2003; Ji et al., 2002; Johnson & Satake, 1999; Kobayashi & Koketsu, 2005; Lay et al., 2005; Mai & Thingbaijam, 2014; Mendoza, 1993, 1995; Mendoza & Hartzell, 1989, 2013; Mendoza et al., 1994; Moreno et al., 2010; Nagai et al., 2001; Okuwaki & Yagi, 2002; Ozawa et al., 2011; Plafker, 1965; Ross et al., 2019;

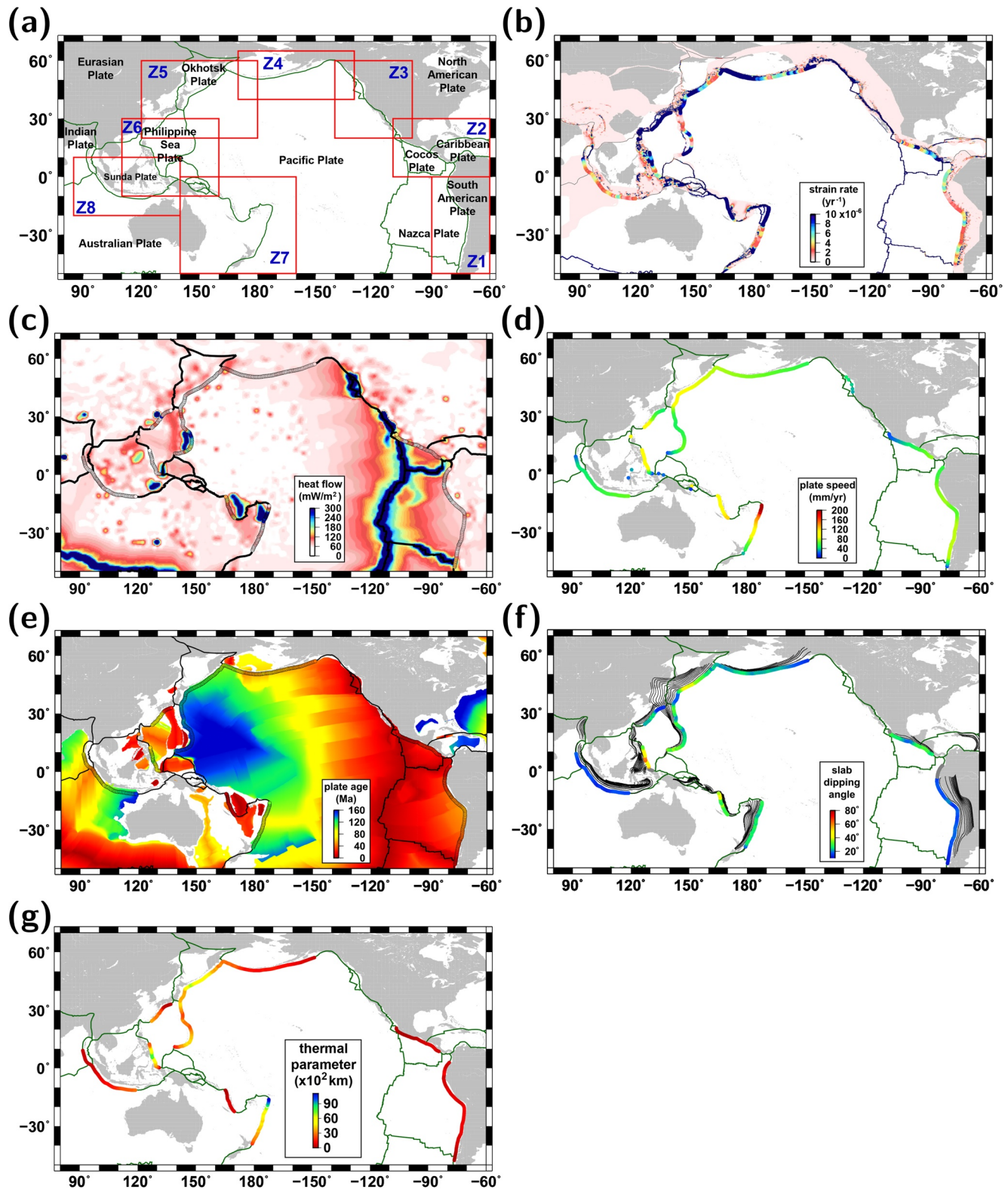


Figure 2. Regional zonation and physical properties along the plate boundaries of the circum-Pacific seismogenic zone: (a) eight subregions, (b) strain rates (Kreemer et al., 2014), (c) heat flows (J. H. Davies, 2013), (d) plate speeds (Ide, 2013), (e) plate ages (Müller et al., 2008), (f) slab dipping angles (Gudmundsson & Sambridge, 1998), and (g) thermal parameters.

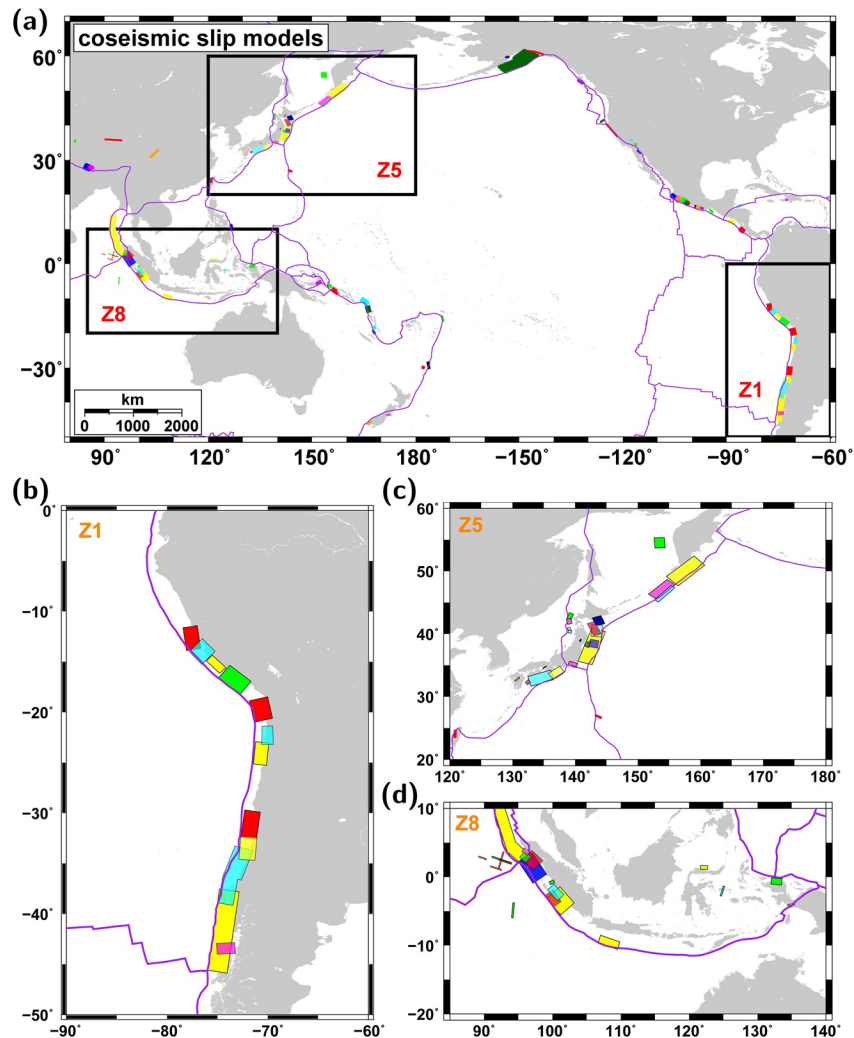


Figure 3. (a) Map of source zones of coseismic slip models for 96 earthquakes with moment magnitudes $\geq M_w 7.0$ in 1900–2020 (Ammon et al., 2005; Asano et al., 2005; Baba et al., 2002; Courboux et al., 1997; Elliott et al., 2010; Fujii & Satake, 2013; Fukuyama & Irikura, 1986; Hartzell & Langer, 1993; Hayes, 2017; Hernandez et al., 2001; Ichinose et al., 2002, 2003; Ji et al., 2002; Johnson & Satake, 1999; Kobayashi & Koketsu, 2005; Mai & Thingbaijam, 2014; Mendoza, 1993, 1995; Mendoza & Hartzell, 1989, 2013; Mendoza et al., 1994; Nagai et al., 2001; Okuwaki & Yagi, 2002; Ross et al., 2019; Sekiguchi et al., 2002; Song et al., 2008; Wald & Heaton, 1994; Yagi, 2004; Yagi et al., 1998; Yamanaka & Kikuchi, 2004; Ye et al., 2013), and enlarged maps of (b) zone 1, (c) zone 5, and (d) zone 8. The source zones of coseismic slip models are marked (rectangles). Different colors are used to distinguish individual source models. The coseismic slip models are applied in the analysis.

Sekiguchi et al., 2002; Song et al., 2008; Wald & Heaton, 1994; Yagi, 2004; Yagi et al., 1998; Yamanaka & Kikuchi, 2004; Ye et al., 2013).

We find that coseismic slip models of 96 large earthquakes with moment magnitudes $\geq M_w 7.0$ in 1900–2020 are available from the resources. We collected the coseismic slip models for the 96 earthquakes (Figure 3). For events with unknown source models (1,540 events), we determine their source parameters (fault dimensions, slip amounts) using empirical scaling laws based on moment magnitudes (Blaser et al., 2010; Mai & Beroza, 2000; Strasser et al., 2010; D. L. Wells & Coppersmith, 1994). Also, we determine unknown fault-plane solutions considering the focal mechanism solutions of adjacent events and subduction-zone geometries. We consider the events are placed adjacent when the events occur on the same subduction plates in consistent slab-interface geometries.

We investigate possible correlations among seismicity, induced stress, and physical parameters in subduction zones to identify the influencing factors in earthquake occurrence at subduction zones. We collect the physical properties around the convergent plate boundaries. The strain rates vary between 0.03 and $96.11 \times 10^{-6} \text{ yr}^{-1}$ (Kreemer et al., 2014) (Figure 2b). The strain rates are 1.05×10^{-6} to $6.65 \times 10^{-6} \text{ yr}^{-1}$ in zone 1, 1.34×10^{-6} to $22.80 \times 10^{-6} \text{ yr}^{-1}$ in zone 2, 1.71×10^{-6} to $26.30 \times 10^{-6} \text{ yr}^{-1}$ in zone 4, 1.93×10^{-6} to $26.45 \times 10^{-6} \text{ yr}^{-1}$ in zone 5, 0.03×10^{-6} to $64.78 \times 10^{-6} \text{ yr}^{-1}$ in zone 6, 1.72×10^{-6} to $96.11 \times 10^{-6} \text{ yr}^{-1}$ in zone 7, and 1.27×10^{-6} to $10.72 \times 10^{-6} \text{ yr}^{-1}$ in zone 8.

The heat flows around the subduction zones vary between 13.0 and 455.8 mW/m^2 (J. H. Davies, 2013) (Figure 2c). The plate convergent speed varies by location from 13 to 236 mm/yr (Ide, 2013) (Figure 2d). The plate convergent speeds are 34.8 – 80.0 mm/yr in zone 1, 22.0 – 75.0 mm/yr in zone 2, 63.0 – 78.8 mm/yr in zone 3, 71.9 – 91.9 mm/yr in zone 4, 18.0 – 111.0 mm/yr in zone 5, 47.0 – 236.0 mm/yr in zone 6, 24.0 – 68.0 mm/yr in zone 7, and 20 – 110 mm/yr in zone 8. The ages of converging plates are typically younger than 160 Ma (Müller et al., 2008) (Figure 2e).

Slab models are collected from a study (Gudmundsson & Sambridge, 1998). The average dipping angles of subducting slabs at depths of less than 50 km are 13.7° to 20.8° in zone 1, 18.4° to 32.3° in zone 2, 20.2° to 25.9° in zone 4, 17.7° to 45.1° in zone 5, 13.0° to 70.0° in zone 6, 17.2° to 42.2° in zone 7, and 13.4° to 18.8° in zone 8 (Figure 2f).

The slab temperature can be approximated using thermal parameters, as well as the product of plate age, trench-normal plate convergence velocity, and the sine of the slab dip angle (Kirby et al., 1996; Maunder et al., 2019; Syracuse et al., 2010). We calculate the thermal parameters (Figure 2g), which is comparable to other studies (Syracuse et al., 2010). The thermal parameters range between 26 and $1,321 \text{ km}$ in zone 1, between 42 and 888 km in zone 2, between 461 and $2,733 \text{ km}$ in zone 4, between $1,361$ and $6,974 \text{ km}$ in zone 5, between $1,262$ and $4,623 \text{ km}$ in zone 6, between 36 and $11,014 \text{ km}$ in zone 7, and between 415 and $2,805 \text{ km}$ in zone 8.

3. Methods

We assess the Coulomb stress changes in subduction zones that may accommodate large earthquakes (Gao & Wang, 2014). The Coulomb stress change, ΔCFS , is determined by (Harris & Simpson, 1998):

$$\Delta\text{CFS} = \Delta\tau + \mu(\Delta\sigma_n + \Delta p), \quad (1)$$

where $\Delta\tau$ is the shear stress change, μ is the frictional coefficient, $\Delta\sigma_n$ is the normal stress change (positive for increased compression), and Δp is the pore fluid pressure change. The frictional coefficient changes with the pore pressure. The static Coulomb stress change can be rewritten by (J. Lin & Stein, 2004; Toda et al., 2005):

$$\Delta\text{CFS} = \Delta\tau + \mu'\Delta\sigma_n, \quad (2)$$

where μ' is the effective frictional coefficient.

We collect the information on the orientation and magnitude of the ambient regional stress field (Zoback, 1992). The ambient stress fields have regionally varying orientations (Zoback, 1992) (see Supporting Information S1). It was reported that the orientations of regional stress fields may play major roles to control the fault-plane orientations and focal mechanisms (King et al., 1994; Toda et al., 1998). Also, the magnitudes of regional stress may affect little on the earthquake triggering as long as they are larger than the earthquake stress drops (King et al., 1994; Toda et al., 1998). Simple uniaxial compressions or extensions with constant magnitudes may be suitable for representation of regional stress field (King et al., 1994). We apply constant magnitudes of principal stress components for calculation of Coulomb stress changes (King et al., 1994; J. Lin & Stein, 2004; Stein et al., 1997; Toda et al., 1998).

The magnitudes of principal stress components are $\sigma_1 = 100 \text{ bar}$, $\sigma_2 = 10 \text{ bar}$, and $\sigma_3 = 0 \text{ bar}$ (King et al., 1994; J. Lin & Stein, 2004; Stein et al., 1997). The maximum and minimum principal stresses (σ_1 , σ_3) are oriented horizontally. The intermediate principal stress is oriented in the vertical direction. The source and medium properties are represented by Young's modulus, Poisson's ratio, and effective coefficient of

Table 1
Relationships Between Rupture Length (R_L), Rupture Width (R_W), and Moment Magnitude (M_W) by Fault Type (D. L. Wells & Coppersmith, 1994)

Fault type	R_L - M_W relationship	R_W - M_W relationship
Strike-slip	$\log(R_L) = -2.57 + 0.62 \cdot M_W$	$\log(R_W) = 3.80 + 2.59 \cdot M_W$
Reverse	$\log(R_L) = -2.42 + 0.58 \cdot M_W$	$\log(R_W) = 4.37 + 1.95 \cdot M_W$
Normal	$\log(R_L) = -1.88 + 0.50 \cdot M_W$	$\log(R_W) = 4.04 + 2.11 \cdot M_W$

friction. The Young's modulus is assumed to be 80 GPa and Poisson's ratio to be 0.25. The shear modulus is based on Young's modulus and Poisson's ratio.

There were numerous studies to investigate the effective frictional coefficients in subduction zones including Japan Trench, Nankai Trough, Kuril Trench, Java Trench, Manila Trench, Kermadec Trench, Middle America Trench (Furukawa & Uyeda, 1989; Gao & Wang, 2014; Harris & Wang, 2002; Harris et al., 2010; Langseth & Silver, 1996; K. Wang & Suyehiro, 1999). The effective frictional coefficients μ' at seismogenic depths (up to ~ 50 km) were reported to be 0.025–0.13, mostly around ~ 0.03 . Thermal structures and frictional heats in subduction faults as well as seismological observations suggest that the effective frictional coefficients may be less than 0.05 in subduction zones (e.g., Cascadia subduction zone, Nankai Trough, Japan Trench, Aleutian Trench, Java Trench, Peru-Chile Trench, Middle America Trench, Mariana Trench, Kermadec Trench, Kuril Trench, Izu-Bonin Trench) (Hippchen & Hyndman, 2008; Magee & Zoback, 1993; Peacock & Wang, 1999; Spinelli & Wang, 2008; von Herzen et al., 2001; Wada & Wang, 2009; K. Wang & He, 1999; K. Wang & Suyehiro, 1999; K. Wang et al., 1995). It is noteworthy that conservative plate boundaries including San Andreas fault zone present similar effective frictional coefficients as low as 0.03–0.04 (Fulton & Saffer, 2009; Gao & Wang, 2017; Williams et al., 2004). In this study, we set the effective frictional coefficient μ' to be 0.03 considering the observed values at seismogenic zones in subduction zones.

We implement coseismic slip models of 96 large earthquakes with moment magnitudes $\geq M_W 7.0$. For events with unknown source parameters, we determine the unknown source parameters (e.g., fault dimensions, slip amounts) using empirical source scaling laws (Blaser et al., 2010; Mai & Beroza, 2000; Strasser et al., 2010; D. L. Wells & Coppersmith, 1994) (Table 1).

We calculated Coulomb stress changes on optimally oriented faults in ambient regional stress field. We stack the Coulomb stress changes induced by large earthquakes. Note that a series of large earthquakes may perturb the static stress field in the medium (Ammon et al., 2008). It is not practically possible to compute continuous cumulative Coulomb stress changes for situations when the geometries of receiver faults in the region are inhomogeneous. We consider a representative receiver fault geometry for a region. To improve the accuracy, we divide the convergent margins by small regions where single representative fault geometries can be considered.

We consider optimally oriented reverse faults at a representative depth of 30 km for presentation of Coulomb stress changes, considering the typical seismogenic depths of megathrust earthquakes in subduction zones (Audet & Kim, 2016). We additionally calculate the Coulomb stress changes for optimally oriented strike-slip faults around the plate boundary between the North American plate and Pacific plate and triple-junction region between Indian, Australian and Sunda plates. Large strike-slip earthquakes often occur in the regions.

The stacking of Coulomb stress changes on a 2-D plane is valid, since the stress induced by a single source decays rapidly with distance. The circum-Pacific seismic zone was discretized by cells with size of 3° -by- 3° . One side of each cell was placed on the plate boundary, and the other sides were placed in inner-trench regions. This configuration of discrete cells enabled the examination of the physical properties of the

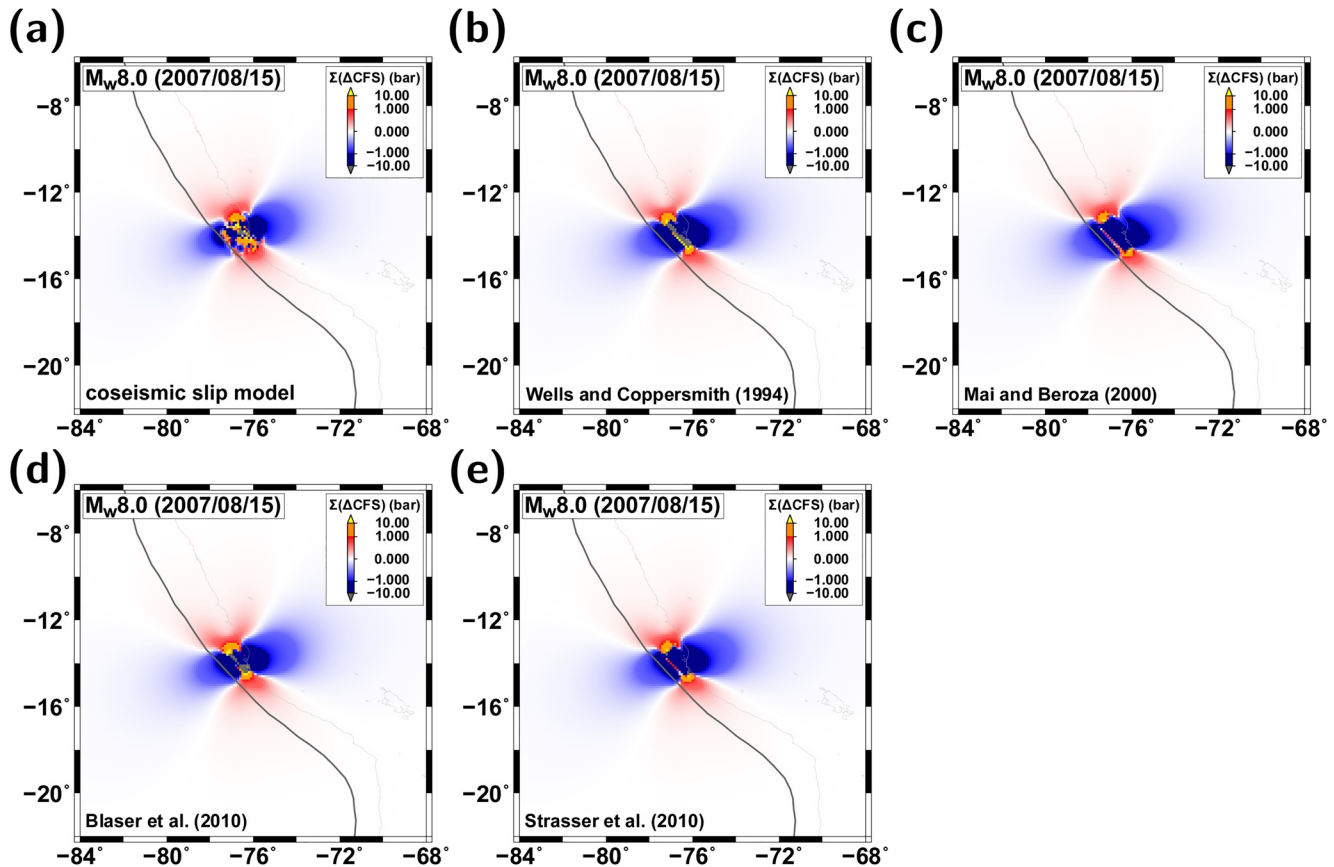


Figure 4. Comparison of Coulomb stress changes induced by the August 15, 2007 M_w 8.0 based on different source models: (a) a coseismic slip model, and homogeneous slip models from (b) the scaling law of D. L. Wells and Coppersmith (1994), (c) the scaling law of Mai and Beroza (2000), (d) the scaling law of Blaser et al. (2010), and (e) the scaling law of Strasser et al. (2010). The Coulomb stress changes are determined similar among the results.

inner-trench regions. The circum-Pacific seismic zone is divided into eight subregions by considering the disposition of major subduction zones (Bird, 2003).

The analysis does not account for natural stress release and temporal compensation, such as viscoelastic medium response, postseismic slips, slow slips, and slow earthquakes. These factors may additionally affect the stress environment (Chan & Stein, 2009; Freed, 2005; Obara & Kato, 2016; Uchida et al., 2016). In this study, we assess only the total magnitudes of stresses induced by large earthquakes since 1900.

4. Analysis of Coulomb Stress Changes

We perform a series of tests to examine the possible variations in the Coulomb stress changes. The Coulomb stress changes may vary by implemented source model. We examine the influence of source slip models on the induced stress fields.

We consider an event with a known coseismic slip model (the August 15, 2007 M_w 8.0 earthquake). We find available scaling laws to determine source parameters based on moment magnitudes (Blaser et al., 2010; Mai & Beroza, 2000; Strasser et al., 2010; D. L. Wells & Coppersmith, 1994). Each scaling law may have own limitation and errors in the assessment of Coulomb stress changes. We compare the Coulomb stress changes based on coseismic slip models with those based on the scaling laws (Figure 4). We determine the source parameters based on four scaling laws (Blaser et al., 2010; Mai & Beroza, 2000; Strasser et al., 2010; D. L. Wells & Coppersmith, 1994). We compare the lateral variations in Coulomb stress changes among different source slip models. We find that all the results are similar (Figure 4). The observation suggests that the Coulomb stress changes based on homogeneous slip models from scaling laws are close to those

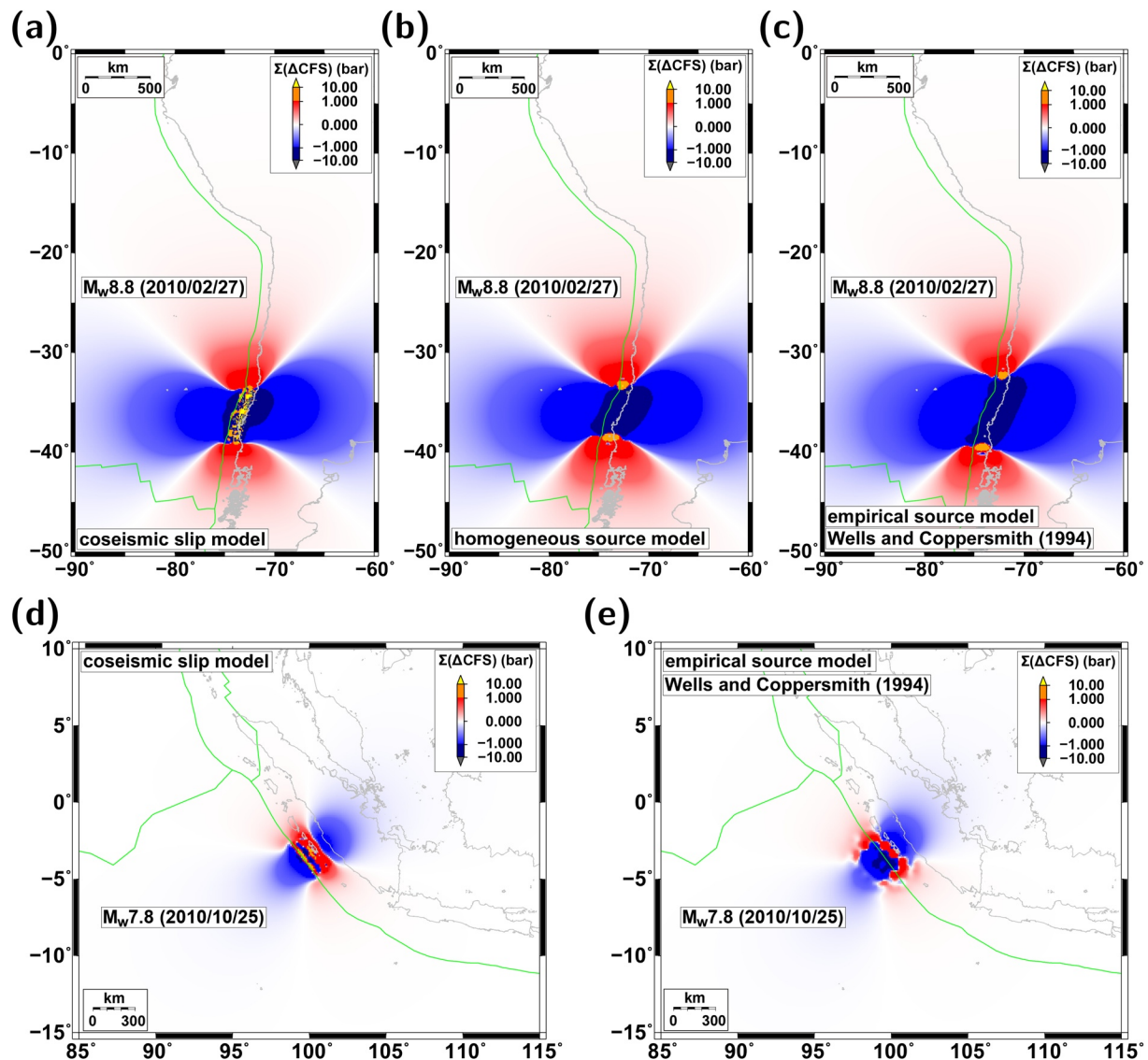


Figure 5. Coulomb stress changes induced by the February 27, 2010 $M_w 8.8$ earthquake based on (a) a coseismic slip model (Hayes, 2017), (b) a homogeneous slip model (Y. N. Lin et al., 2013), and (c) source parameters from empirical relationships (D. L. Wells & Coppersmith, 1994). Coulomb stress changes induced by the 25 October $M_w 7.8$ earthquake based on (d) a coseismic slip model (Hayes, 2017), and (e) source parameters from empirical relationships (D. L. Wells & Coppersmith, 1994). The estimated Coulomb stress changes are similar among the models.

based on coseismic slip models (Figure 4). Further, the different scaling laws rarely introduce noticeable differences in the results.

We additionally consider two other events (the February 27, 2010 $M_w 8.8$ earthquake, the October 25, 2010 $M_w 7.8$ earthquake) (Figure 5). We implement three types of source slip models that include coseismic slip models, homogeneous slip models based on known source dimensions, and homogeneous slip models based on the scaling laws. We choose one representative scaling law (D. L. Wells & Coppersmith, 1994) for the calculation of Coulomb stress changes of events with unknown coseismic slip models. The observation suggests that simplified slip models may be applicable for regional assessment of stress perturbation. Hereafter, we use the scaling laws of D. L. Wells and Coppersmith (1994) for analysis of events with unknown source parameters.

The detailed geometry of plate interfaces are not fully known. It is practically useful to consider optimally oriented faults. However, the orientations of receiver faults may control the induced stress field. We

examine the optimal-orientations of receiver faults. Also, the Coulomb stress changes are calculated for the optimally oriented receiver faults. We find that the orientations of optimally oriented faults are generally consistent with the local slab-interface geometries even around triple junctions (Figure 6).

We additionally compare the cumulative Coulomb stress changes for receiver faults in optimal orientations with those for receiver faults in given orientations following local tectonic structures (Figures 7a–7c). We observe that the overall features in cumulative Coulomb stress changes are similar between the two cases. The observations suggest that the Coulomb stress changes for optimally oriented receiver faults may enable us to assess the regional induced stress fields reasonably.

We conduct additional tests to examine the validity of the method. We assess the cumulative Coulomb stress changes along the Peru-Chile Trench using the proposed method (Figures 8a–8d). We also calculate the cumulative Coulomb stress changes in three selected regions (regions d1, d2, d3) for given receiver-fault orientations that are set to be trench-parallel (Figures 8e–8g). We measure the differences of cumulative Coulomb stress changes between two approaches. The differences are negligibly small compared to the levels of cumulative Coulomb stress changes (Figures 8h–8j). The observation suggests that the proposed method based on optimal receiver-fault orientations yields reasonable results. Also, the proposed method covers the study area in consistent manner, yielding continuous cumulative Coulomb stress changes in regions.

We examine the influence of effective frictional coefficient on the regional induced stress field. We compare the cumulative Coulomb stress changes for different effective frictional coefficients ($\mu' = 0.03, 0.4$) (Figures 7b and 7d). The regional variations in cumulative Coulomb stress changes are close between the two cases. In this study, we implement the effective frictional coefficient of $\mu' = 0.03$.

5. Cumulative Coulomb Stress Changes

We calculate long-term cumulative Coulomb stress changes induced by 1,636 earthquakes (1,457 earthquakes with moment magnitudes $\geq M_w 7.0$, and 179 earthquakes with moment magnitudes $M_w 6.4$ – 6.9) in 1900–2020. The cumulative Coulomb stresses evolve with time due to continuous occurrence of large earthquakes. The Coulomb stress changes are calculated for optimally oriented reverse faults around the circum-Pacific seismic zone.

Major earthquakes produce lateral heterogeneities in the induced stress fields around active plate margins. The cumulative Coulomb stress changes vary between -337.5 and 697.9 bar around the circum-Pacific seismic zones (Figure 9). Negative cumulative Coulomb stress changes were generally dominant in the subduction zones, suggesting that the loaded stresses were released by precedent nearby earthquakes. Large positive cumulative Coulomb stress changes suggest that the static stresses transferred from neighboring regions are accumulated without faulting.

Large Coulomb stress changes occur after large earthquakes. Large slip deficits occur in numerous subduction zones (Graham et al., 2016; Hashimoto et al., 2009; Ikuta et al., 2015; Koyama et al., 2012; Li & Freymueller, 2017; Loveless & Meade, 2010; Pulido et al., 2014; Widiyantoro et al., 2020; Yamazaki et al., 2014). We observe large positive cumulative Coulomb stress changes at some interseismic locking zones with large slip deficits in subduction zones including the northern and central Peru-Chile Trench in zone 1, Middle America Trench in zone 2, Aleutian Trench in zone 4, Nankai Trough, Japan Trench, and Kuril Trench in zone 5, Ryukyu Trench in zone 6, New Hebrides Trench, and Kermadec Trench in zone 7, Java Trench in zone 8.

The overall cumulative Coulomb stress changes are generally comparable among different subduction zones. Great earthquakes dominantly perturb the long-term cumulative Coulomb stress changes (Figure 10). Comparable levels of cumulative Coulomb stress changes are achieved long after the occurrence of large earthquakes. This observation suggests that the stress changes induced by precedent earthquakes may be comparable among subduction zones.

We calculate the cumulative Coulomb stress changes for earthquakes with moment magnitudes $\geq M_w 7.0$. These large earthquakes dominantly affect the regional stress fields. For comparison, we additionally calculate the cumulative Coulomb stress changes induced by earthquakes with magnitudes $\geq M_w 8.0$ and

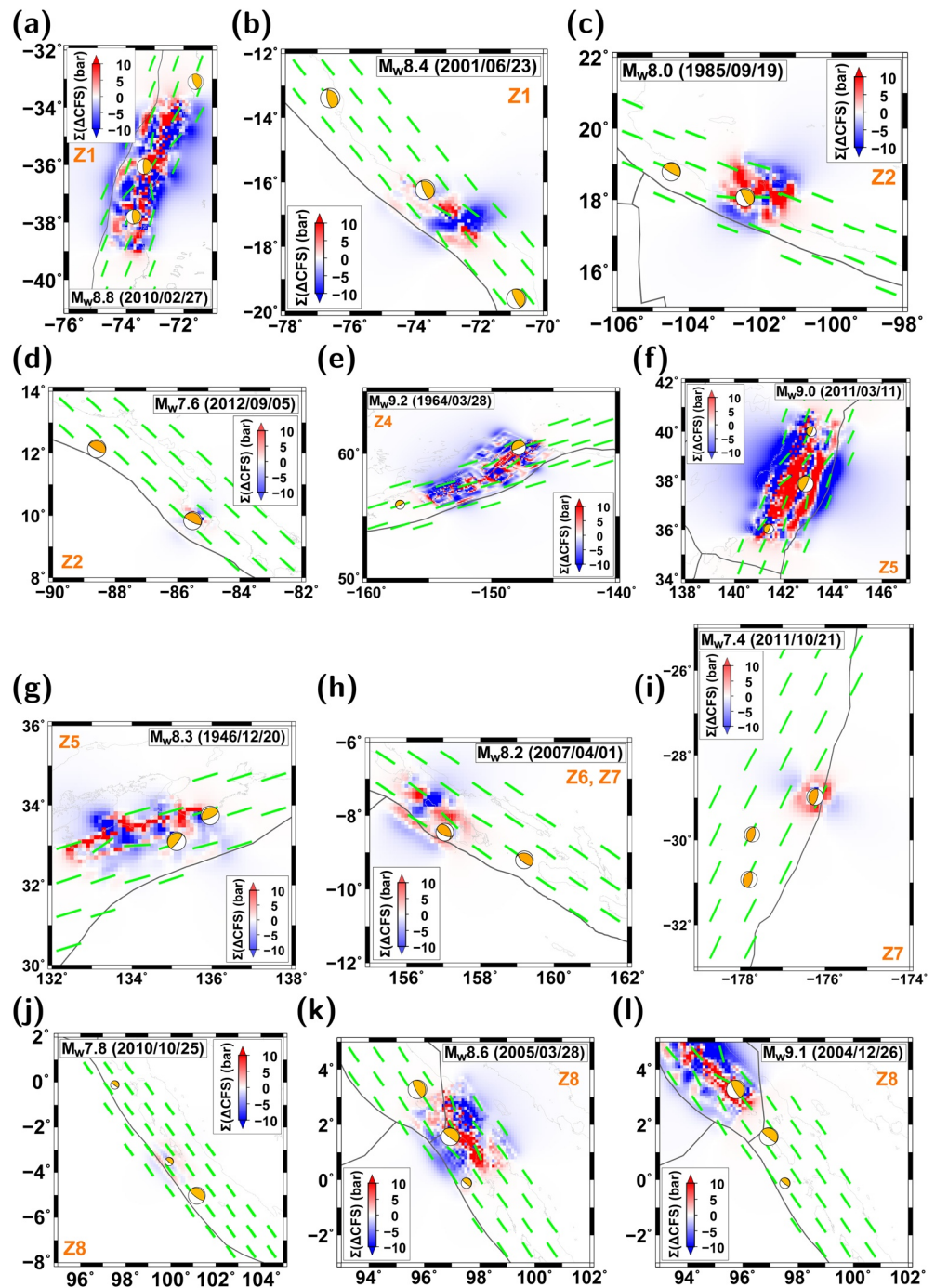


Figure 6. Coulomb stress changes induced by single large earthquakes and optimal fault-plane orientations of receiver reverse faults: (a) the February 27, 2010 M_w 8.8 earthquake in zone 1, (b) the June 23, 2001 M_w 8.4 earthquake in zone 1, (c) the September 19, 1985 M_w 8.0 earthquake in zone 2, (d) the September 5, 2012 M_w 7.6 earthquake in zone 2, (e) the March 28, 1964 M_w 9.2 earthquake in zone 4, (f) the March 11, 2011 M_w 9.0 earthquake in zone 5, (g) the December 20, 1946 M_w 8.3 earthquake in zone 5, (h) the April 1, 2007 M_w 8.2 earthquake in zones 6 and 7, (i) the October 21, 2011 M_w 7.4 earthquake in zone 7, (j) the October 25, 2010 M_w 7.8 earthquake in zone 8, (k) the March 28, 2005 M_w 8.6 earthquake in zone 8, and (l) the December 26, 2004 M_w 9.1 earthquake in zone 8. The focal mechanism solutions of a couple of earthquakes are presented for comparison. The optimal fault-plane orientations of receiver reverse faults (broken lines) are generally trench-parallel.

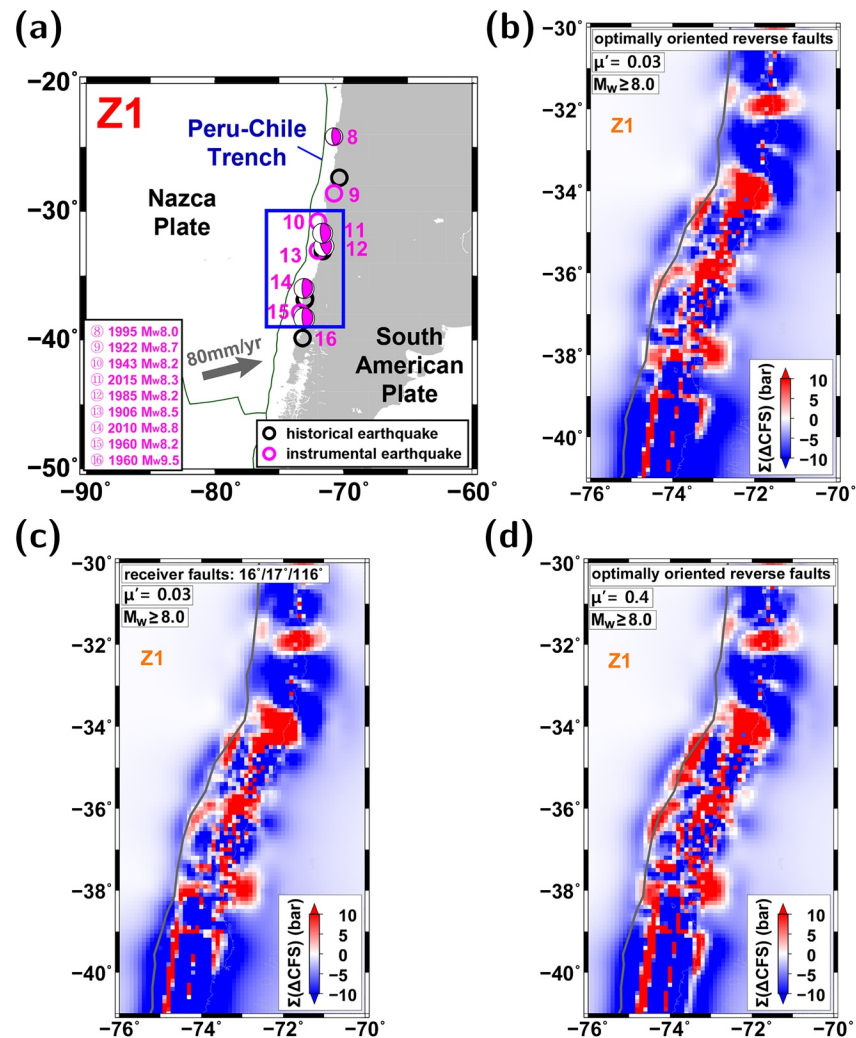


Figure 7. Comparison of cumulative Coulomb stress changes for different receiver-fault orientations: (a) Map of study region and earthquakes, (b) cumulative Coulomb stress changes for optimally oriented thrusts with effective frictional coefficient $\mu' = 0.03$, (c) those for thrusts with a given trench-parallel orientation and $\mu' = 0.03$, and (d) those for optimally oriented thrusts with $\mu' = 0.4$. The study region is marked on the map (rectangle). The cumulative Coulomb stress changes are similar among different cases.

$\geq M_w 6.5$ (Figure 11). We observe that the cumulative Coulomb stress changes are mainly controlled by large events. The cumulative Coulomb stress changes for earthquakes with magnitudes $\geq M_w 6.5$ are close to those for earthquakes with magnitudes $\geq M_w 7.0$. The observation suggests that the cumulative Coulomb stress changes for earthquakes with moment magnitudes $\geq M_w 7.0$ may present major stress perturbations.

The faulting mechanisms and stress systems are different between subduction zones and outer-rise regions. The stress fields in the outer-rise regions are composed of trench-normal tensions. On the other hand, trench-normal compression is active on slab interface. We investigate the seismicity and stress field changes on slab interfaces at seismogenic depths where major earthquakes nucleate. We confined the study regions along subduction zones (Figure 9).

6. Correlation With Tectonic Properties

We examine the dependency of the cumulative Coulomb stress changes on tectonic properties such as strain rates, heat flows, and thermal parameters (J. H. Davies, 2013; Kreemer et al., 2014; Maunder et al., 2019). We sort the cumulative Coulomb stress changes along plate boundaries as a function of strain rates, heat flows,

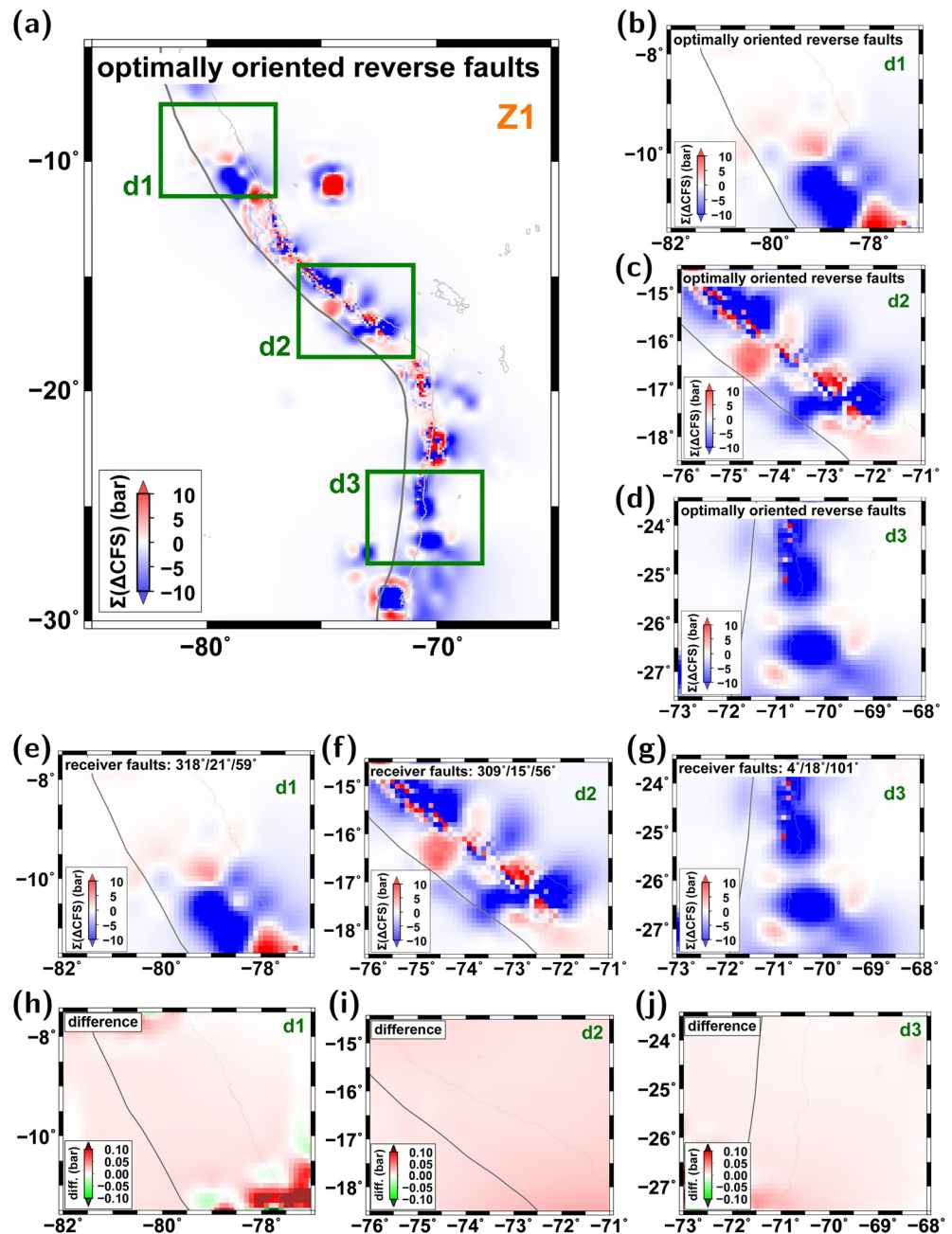


Figure 8. Comparison of cumulative Coulomb stress changes for three local regions (d1, d2, d3) in zone 1: (a) map of local regions and cumulative Coulomb stress changes for optimally oriented thrusts, (b) enlarged views for region d1, (c) region d2, and (d) region d3. Cumulative Coulomb stress changes for thrusts with a given trench-parallel orientation (e) in region d1, (f) region d2, and (g) region d3. Differences between the cumulative Coulomb stress changes for optimally oriented thrusts and those for trench-parallel-oriented thrusts (h) in region d1, (i) region d2, and (j) region d3. The cumulative Coulomb stress changes are determined similar between the two cases. The differences of cumulative Coulomb stress changes are small.

and thermal parameters. We determine the averages and standard deviations of cumulative Coulomb stress changes (Figure 12). The cumulative Coulomb stress changes are observed to be minimally dependent on the physical properties (Figure 12).

We find both positive and negative stress changes, but not zero stress changes, at common magnitudes of physical parameters. This feature may develop due to spatially inhomogeneous occurrence of major

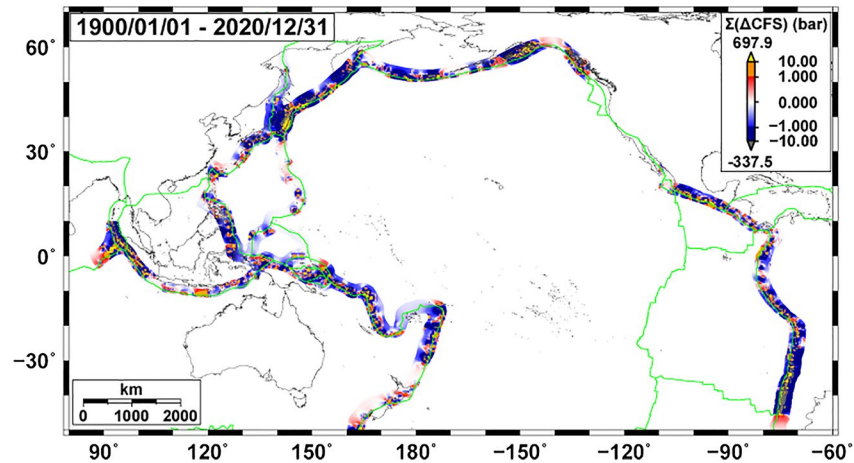


Figure 9. Cumulative Coulomb stress changes induced by 1,636 earthquakes combining 1,457 earthquakes with moment magnitudes greater than or equal to M_w 7.0 and 179 earthquakes with moment magnitudes M_w 6.4–6.9 in 1900–2020. The Coulomb stress changes were calculated for optimally oriented thrusts. The cumulative Coulomb stress changes are laterally heterogeneous along plate boundaries.

earthquakes. The differences between positive and negative cumulative Coulomb stress changes are on the order of tenths to tens of bar, producing large lateral heterogeneities in stress fields. The absolute magnitudes of peak positive and negative Coulomb stress changes do not exceed 100 bar. This observation suggests that the stress induced from adjacent earthquakes may possibly recover the coseismic stress decreases of the faults.

7. Seismicity Feature in Subduction Zones

Six great earthquakes with moment magnitudes greater than M_w 8.5 occurred on the subduction zones from 2004 to 2012. The long-term cumulative Coulomb stress changes are dominantly controlled by precedent great earthquakes that significantly perturb media up to regional distances (Hong et al., 2015; Hong, Lee, Chi, et al., 2017). Large earthquakes induce stress decreases (negative Coulomb stress changes) in the fault-ruptured regions. It was reported that seismicity increases in elevated-stress regions (Hong et al., 2018, 2020; Hong, Lee, Kim, et al., 2017; King et al., 1994; Nalbant et al., 1998; Stein et al., 1997; Toda et al., 2005).

We examine the seismicity dependency on cumulative Coulomb stress changes. We assess the cumulative Coulomb stress changes along subduction zones during 1900–2012. The cumulative Coulomb stress changes during 1900–2012 are compared with the seismicity of moderate-size earthquakes with moment magnitudes of 4.0–5.0 in the following year, 2013 (Figure 13). We present the moment releases of moderate-size earthquakes as a function of Coulomb stress change (Figure 13). The data points are sorted by strain rates, heat flows, and thermal parameters of the regions.

We consider only the slab interface regions. We discretize the circum-Pacific seismic zone by cells with a uniform size of 3° -by- 3° . One sides of cells are placed on the plate boundary. The other sides are placed in inner-trench regions. This configuration of discrete cells enables us to compare various physical properties, seismicity, seismic moments with Coulomb stress changes on the slab interface in the inner-trench regions.

The released energy of postseismicity in the stress-increase regions presents negligible apparent correlation with the magnitude of induced stress (left column in Figure 13). The magnitude of induced seismicity appears to be independent of the strength of induced stress, as long as the induced stress is greater than 0.01 bar (Figure 13). This observation may indicate the lower bound of induced stress necessary to trigger earthquakes, which is consistent with other studies (Helmstetter & Shaw, 2006, 2009).

It is intriguing to note that moderate-size earthquakes occur more commonly in the stress-decrease regions than in the stress-increase regions (Figure 13). More earthquakes occur in the regions of greater stress-decrease, which is evident according to the perspective of any common physical parameters. This feature

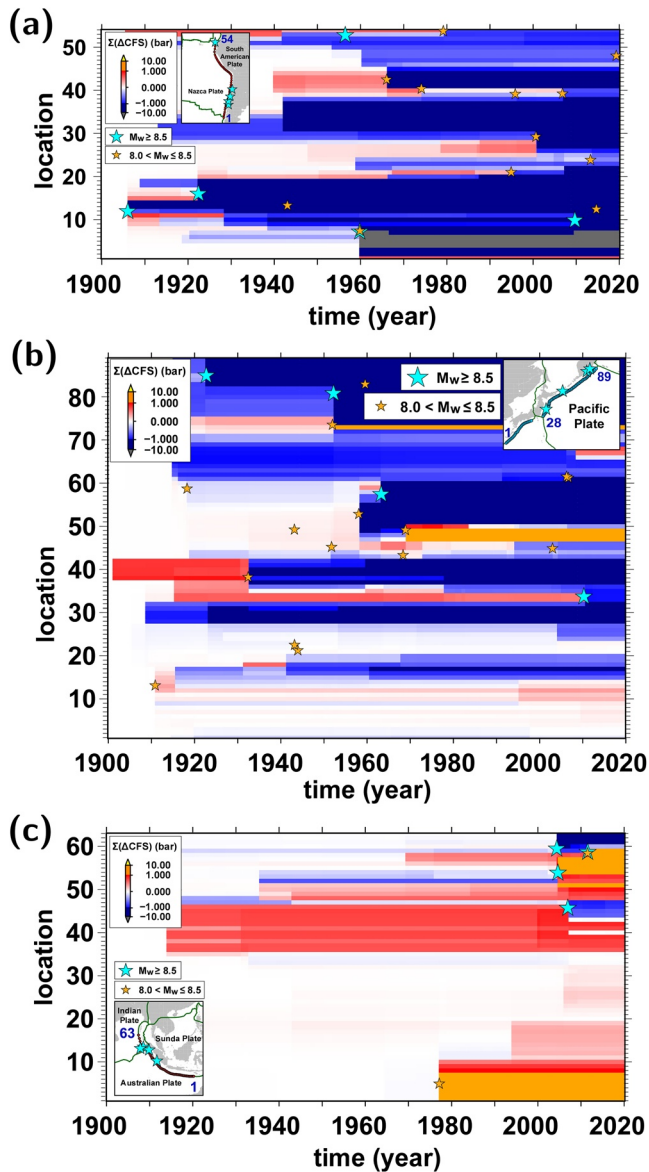


Figure 10. Temporal evolution of cumulative Coulomb stress changes around the (a) Peru-Chile Trench, (b) Kuril and Japan Trenches, and (c) Java Trench. The cumulative Coulomb stress changes vary significantly after great earthquakes. The occurrence times of large earthquakes are marked (stars).

may be attributed to the fact that postseismicity is concentrated in the fault-ruptured source regions that accompany coseismic stress drops.

The apparent correlation between the negative cumulative Coulomb stress changes and postseismic moderate-size earthquakes may be associated with the medium weakening after large earthquakes. The frictional resistance and yield strength may be decreased by the medium perturbation (Cattin et al., 2009), inducing more earthquakes as a result of postseismic medium responses. Viscoelastic relaxation of media after large earthquakes may additionally foster the seismicity (Chan & Stein, 2009). These observations suggest that the ruptured slab interface may incorporate more moderate-size earthquakes (Wada et al., 2008).

8. Large Earthquake Induction

We examine the large-earthquake occurrence with temporal evolution of cumulative Coulomb stress change in plate boundaries. We choose large earthquakes with moment magnitudes greater than 8.0 from representative subduction zones. We assess the cumulative Coulomb stress changes 3 months before the events.

The February 27, 2010 M_w 8.8 Maule Chile earthquake occurred in a region with a large variation of static stress ranging -3 to 8 bar which corresponds to a preseismic locking zone in the Peru-Chile Trench off central Chile (Figure 14a). The megathrust earthquake lowered the static stress level around the epicentral region that had accumulated since the last megathrust event in 1835 (Moreno et al., 2010). The 2010 M_w 8.8 earthquake loaded the stress in the subduction zone of latitude of -36° to -34° . The April 1, 2014 M_w 8.1 earthquake occurred in the Peru-Chile Trench off northern Chile in a region with large static stress variation (Figure 14b). The September 16, 2015 M_w 8.3 earthquake occurred in a region of localized stress contrasts (Figure 14c). The September 16, 2015 M_w 8.3 earthquake lowered the stress level in the region.

A large lateral variation of static shear stress was observed in the Japan Trench off eastern Hokkaido, Japan before the September 25, 2003 M_w 8.3 Tokachi-Oki earthquake (Figure 15a). The earthquake lowered the elevated-stress level in the region. In addition, a persistent stress contrast of ± 12 bar in the Japan Trench off Tohoku was relieved by the March 11, 2011 M_w 9.0 earthquake (Figure 15b). The earthquake lowered the stress level over a wide region along the trench. On the other than, the earthquake increased the stress contrasts in the source zone (rupture area). The increased stress in the rupture area produced successive aftershocks.

The December 26, 2004 M_w 9.1 Sumatra-Andaman earthquake occurred in the boundary between the Indo-Australian plate and the Sunda plate near northwestern Sumatra, Indonesia. The earthquake occurred in a region with 110 km radius with a large spatial variation in cumulative Coulomb stress changes ranging -0.9 to 1.1 bar (Figure 16a). The rupture initiated at the location of stress contrast (Figure 16). The earthquake lowered the static stress level in the epicenter region, while increasing the static stress level in a region of the Java Trench where a M_w 8.6 event occurred 3 months later (Figure 16b). A M_w 8.5 event occurred ~ 30 months later in a region of elevated stress located southeast of the 2004 M_w 9.1 earthquake (Figure 16c).

The successive stress transfer from the large events in the subduction zones triggered the April 11, 2012 M_w 8.6 strike-slip earthquake (Figure 17a). It is noteworthy that the M_w 8.6 earthquake location corresponds to a region of large gradient in cumulative stress field (large stress contrast). The M_w 8.6 strike-slip event

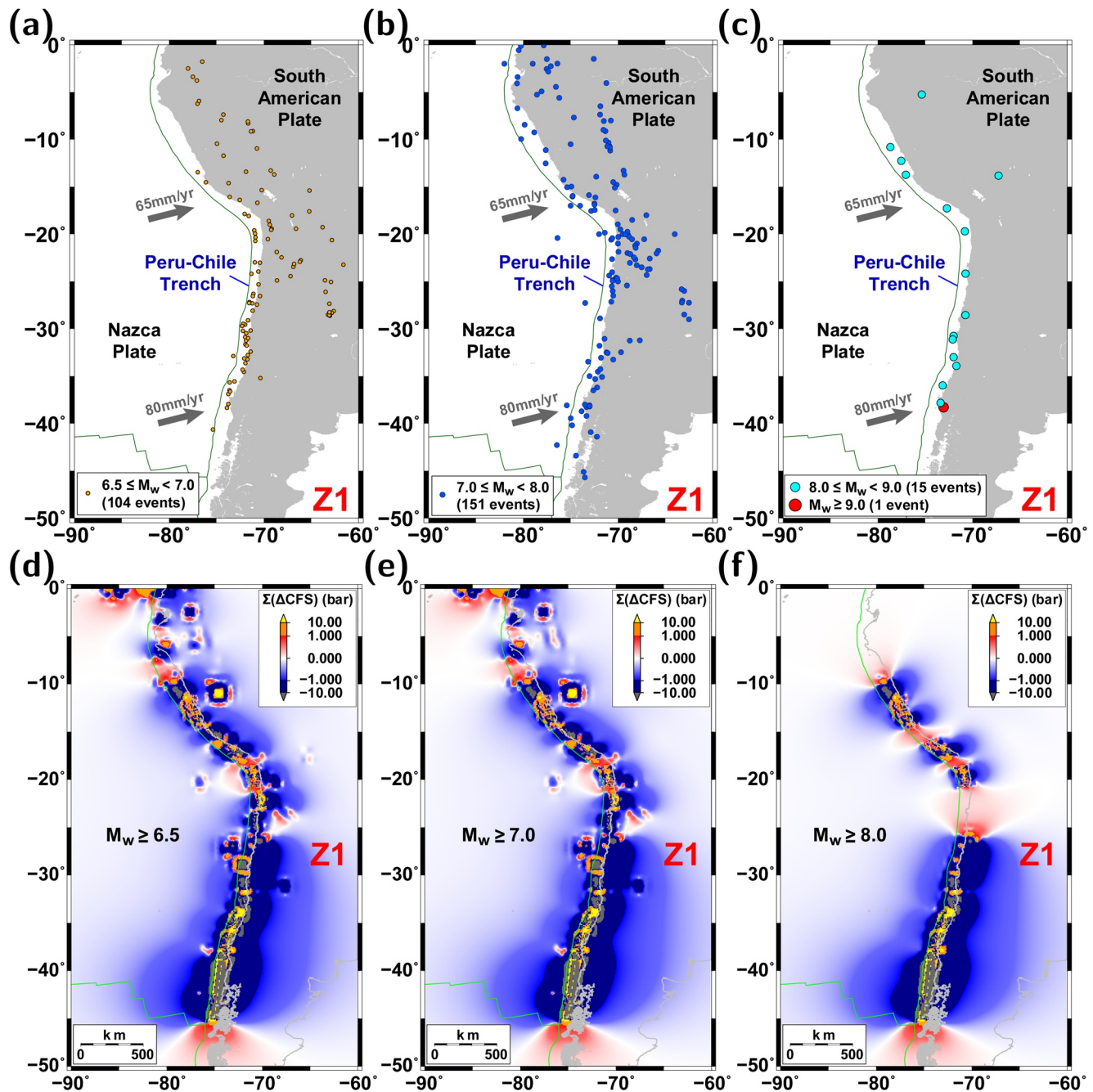


Figure 11. Distribution of earthquakes with magnitudes of (a) $6.5 \leq M_w < 7.0$, (b) $7.0 \leq M_w < 8.0$, and (c) $M_w \geq 8.0$ in zone 1. The numbers of events are indicated. Cumulative Coulomb stress changes induced by earthquakes with moment magnitudes greater than or equal to (d) $M_w 6.5$, (e) $M_w 7.0$, and (f) $M_w 8.0$ in zone 1.

increased the Coulomb stress on optimally oriented strike-slip faults in the region around the epicenter, causing a significant increase of aftershocks (Figure 17b).

The $M_w 8.6$ earthquake triggered the $M_w 8.2$ earthquake 2 h later (Figure 17c). The two large strike-slip earthquakes perturbed the stress field around the outer-rise, inducing the seismicity in adjacent regions. This observation suggests that stress field perturbation by reverse-faulting earthquakes can induce strike-slip earthquakes.

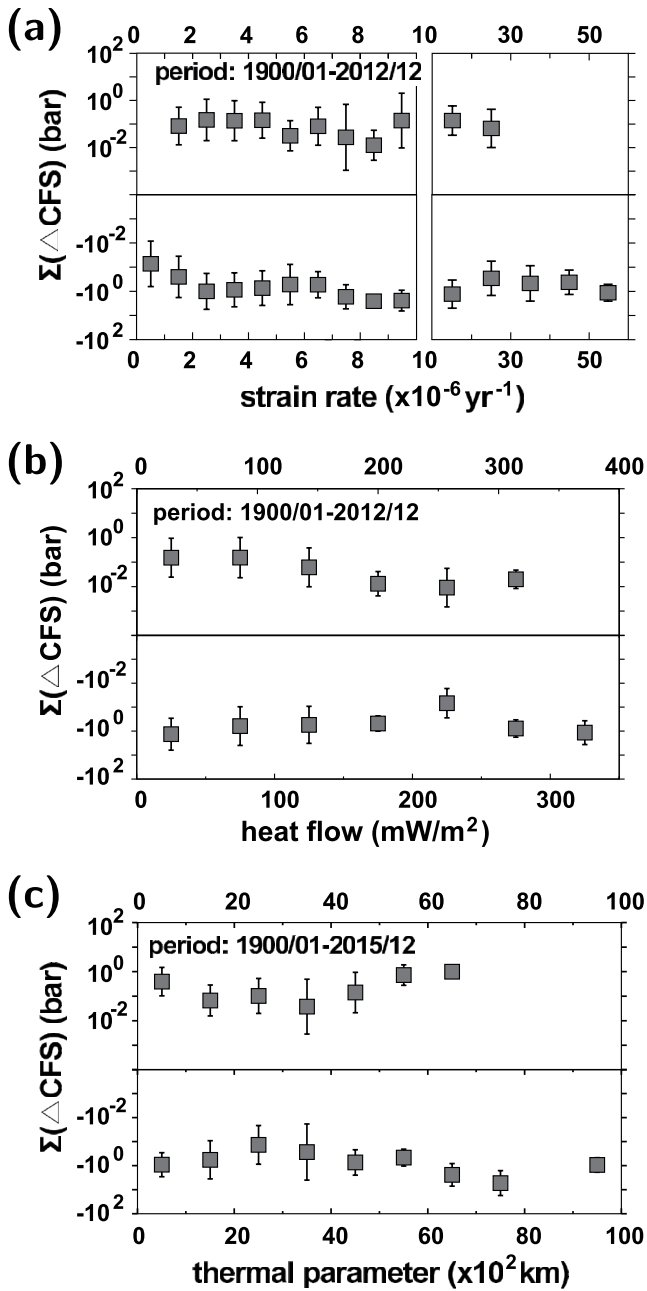


Figure 12. Variation of cumulative Coulomb stress changes ($\Sigma(\Delta CFS)$) during 1900–2020 as a function of (a) strain rate, (b) heat flow, and (c) thermal parameters. The standard deviations (bars) are presented. The cumulative Coulomb stress changes are barely dependent on the magnitudes of subduction zone properties.

We examine the lateral variations in induced stress fields of large earthquakes. We choose representative subduction zones including Peru-Chile Trench (zone 1), Middle America Trench (zone 2), Japan Trench and Nankai Trough (zone 5), South Solomon Trench and Tonga Trench (zone 7), and Java Trench (zone 8) (Figure 18a). There are 22 earthquakes with magnitudes $\geq M_w 8.0$ since 2000. Fifteen earthquakes out of 22 earthquakes occurred on slab interfaces. The other seven events are deep-focus earthquakes, outer-trench earthquakes, or intraplate earthquakes. We find 15 large subduction-zone earthquakes with magnitudes $\geq M_w 8.0$ since 2000. We analyze all the 15 large subduction-zone events.

The 15 events include the February 27, 2010 $M_w 8.8$ Maule earthquake (event A1), the September 16, 2015 $M_w 8.3$ Illapel earthquake (event A2), the April 1, 2014 $M_w 8.1$ Iquique earthquake (event A3), the June 23, 2001 $M_w 8.4$ Arequipa earthquake (event A4), the August 15, 2007 $M_w 8.0$ Pisco earthquake (event A5), the September 8, 2017 $M_w 8.1$ Chiapas earthquake (event A6), the March 11, 2011 $M_w 9.0$ earthquake (event B1), the September 25, 2003 $M_w 8.3$ earthquake (event B2), the November 15, 2006 $M_w 8.3$ Kuril Islands earthquake (event B3), the December 26, 2004 $M_w 9.1$ Sumatra-Andaman earthquake (event C1), the March 28, 2005 $M_w 8.6$ Nias-Simeulue earthquake (event C2), the September 12, 2007 $M_w 8.5$ Southern Sumatra earthquake (event C3), the December 23, 2004 $M_w 8.1$ Macquarie Island earthquake (event D1), the May 3, 2006 $M_w 8.0$ Tonga earthquake (event D2), and the April 1, 2007 $M_w 8.2$ Solomon Islands earthquake (event D3) (Figure 18).

Earthquakes generally nucleate at point locations, rupturing outward from the nucleation locations (hypocenters) along fault planes. We examine the lateral stress distribution in the hypocentral areas. We measure the stress contrasts in source regions by estimating the peak stress difference along fault planes in the earthquake hypocentral regions with a radius of 100 km.

The source region of the February 27, 2010 $M_w 8.8$ Maule earthquake presents the peak lateral stress change of 11 bar in the trench-parallel direction (Figure 18c). The September 16, 2015 $M_w 8.3$ Illapel earthquake present peak lateral stress changes of ~ 34 bar in the trench-parallel direction (Figure 18d). The source region of the March 11, 2011 $M_w 9.0$ Tohoku-Oki earthquake displays the peak lateral stress change of 24 bar in the trench-parallel direction (Figure 18i). Similarly, the source region of the September 25, 2003 $M_w 8.3$ Tokachi-Oki earthquake present a stress contrast as large as ~ 16 bar (Figure 18j). The December 26, 2004 $M_w 9.1$ Sumatra-Andaman earthquake occurred in a region with peak lateral stress change of 2 bar in the trench-parallel direction (Figure 18l). The source region of the September 12, 2007 $M_w 8.5$ earthquake displays the peak lateral stress change of 18 bar in the trench-parallel direction (Figure 18n).

We consistently find that the large earthquakes occurred in the regions of high stress contrasts. We find that 12 events out of 15 events present stress contrasts as large as 7–24 bar in the hypocentral regions before the earthquakes (Figure 18b). It is noteworthy that the other three events (events A3, A6, C1) have stress contrasts of 1–4 bar due to low seismicity (none to two $M 7$ earthquakes since 1900) before the earthquakes. The stress field in the three event regions was little perturbed by adjacent earthquakes for last 120 years.

It is noteworthy that the stress contrasts of several to tens of bars are noticeable magnitudes considering the deviatoric stress level in regional stress field (~ 100 bar). A series of large earthquakes may induce

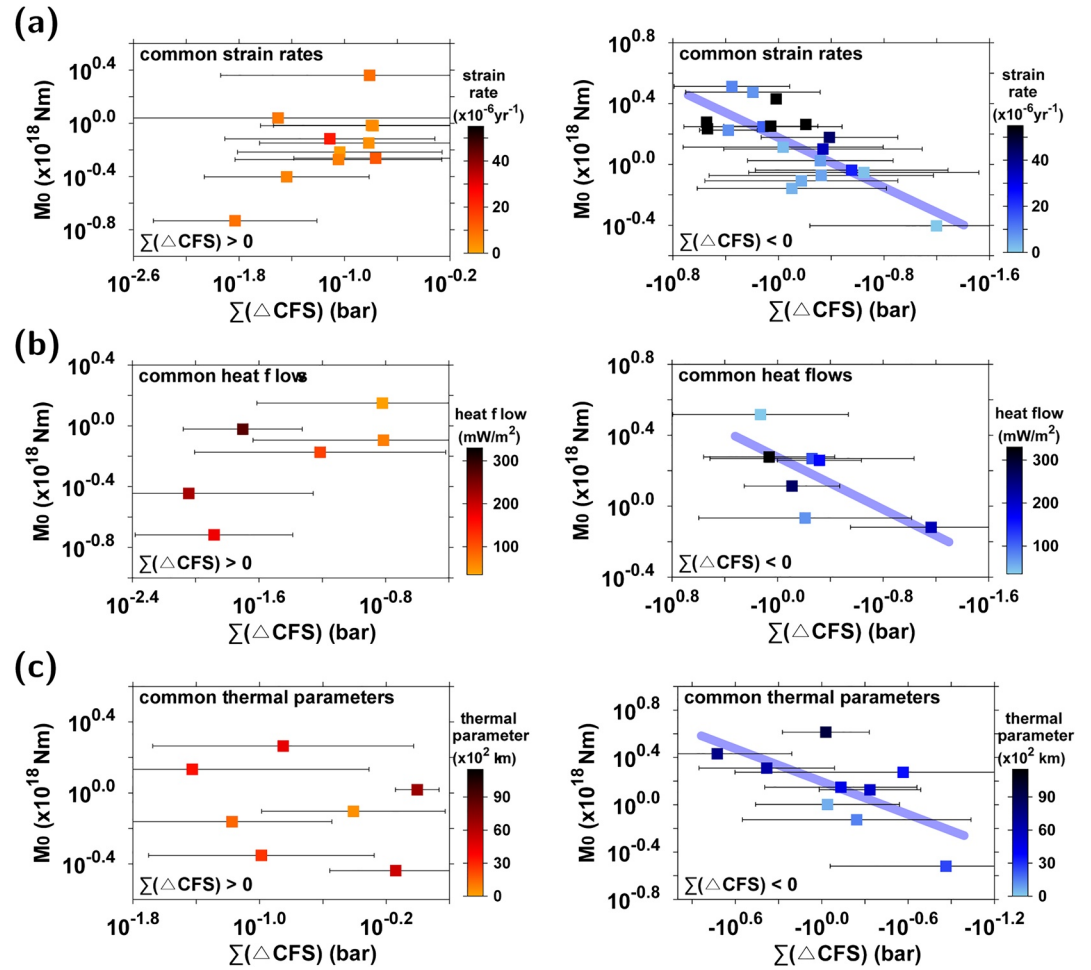


Figure 13. Total seismic moments (M_0) released from moderate-size earthquakes in 2013 as a function of cumulative Coulomb stress changes ($\Sigma(\Delta CFS)$) by precedent earthquakes in 1900–2012 for common (a) strain rate, (b) heat flow, and (c) thermal parameters. Comparisons are presented for stress-increase (left column) and stress-decrease (right column) regions. Strong linear correlations are observed between seismic moments of postseismicity and cumulative Coulomb stress changes in stress-decrease regions due to seismic events during postseismic slips. The correlations are relatively weak in stress-increase regions.

noticeable stress perturbations in adjacent regions. Also, the observation may suggest that large earthquakes may generally occur in the regions with large lateral gradients in induced stress fields (Figure 18). Thus, the stresses transferred from adjacent events may trigger earthquakes successively. This feature is observed globally on plate boundaries, regardless of the tectonic properties. Earthquakes for long terms may induce heterogeneous local stress field. The large postseismic earthquakes may be substantially affected by precedent large earthquakes.

9. Regional Variation in Induced Stress Fields

We consider eight subregions around the circum-Pacific seismic zone (Figure 2a). The cumulative Coulomb stress changes varied between -337.5 and 333.7 bar in zone 1, between -81.92 and 48.62 bar in zone 2, between -34.20 and 194.5 bar in zone 4, between -207.3 and 697.9 bar in zone 5, between -41.81 and 34.08 bar in zone 6, between -96.43 and 96.57 bar in zone 7, and between -180.9 and 649.9 bar in zone 8. The cumulative Coulomb stress changes varied between -21.71 and 47.98 bar in the western North American plate (zone 3) for optimally oriented strike-slip faults that were dominant in the region.

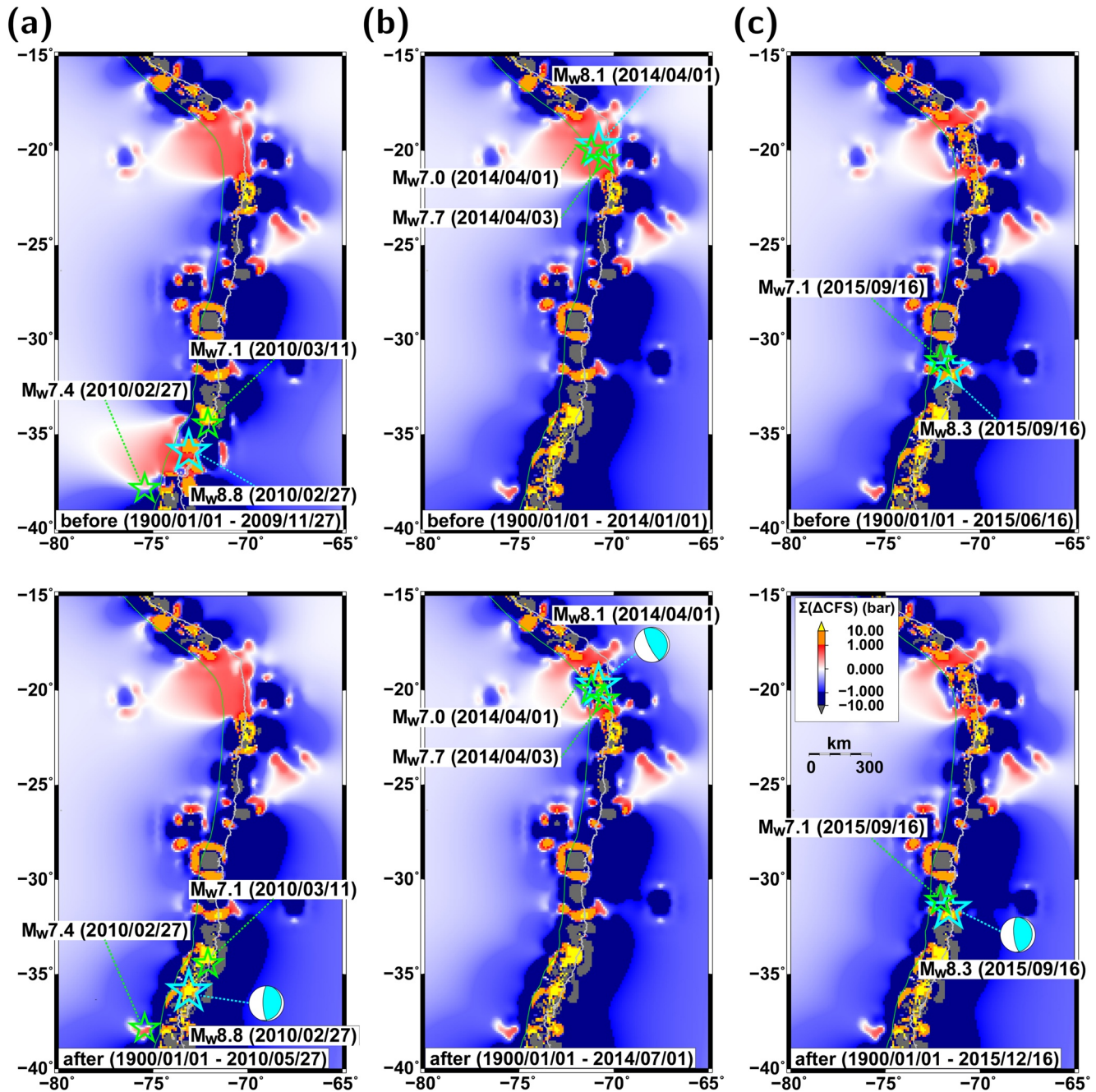


Figure 14. Temporal evolution of cumulative Coulomb stress changes for optimally oriented reverse faults around the Peru-Chile Trench before and after (a) the February 27, 2010 M_w 8.8 earthquake, (b) the April 1, 2014 M_w 8.1 earthquake, and (c) the September 16, 2015 M_w 8.3 earthquake. The cumulative stress fields 3 months before (upper column) and after (lower column) the mainshocks are presented. The mainshock locations and calculation periods are denoted. The mainshocks primarily occurred in the regions around high stress gradients.

9.1. Zone 1

Megathrust earthquakes occur frequently along the Peru-Chile Trench, producing large lateral perturbations in stress fields (Figure 19). There are seismic gaps in the northern Peru-Chile Trench at latitudes of -10° to -4° , and in the central Peru-Chile Trench at latitudes of -23° to -18° (Delouis et al., 2007; Hayes et al., 2014; Villegas-Lanza et al., 2016).

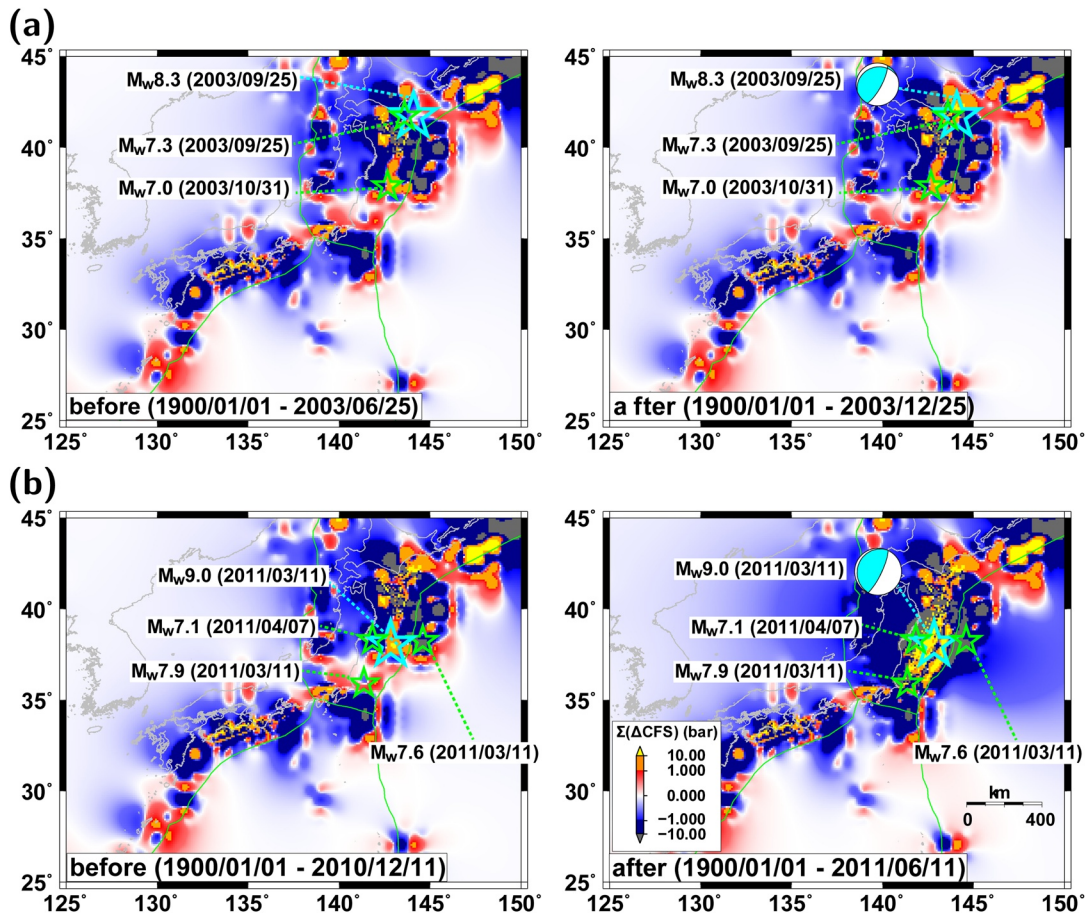


Figure 15. Temporal evolution of cumulative Coulomb stress changes for optimally oriented reverse faults around the Kuril, Japan and Ryukyu Trenches before and after (a) the September 25, 2003 M_w 8.3 earthquake and (b) the March 11, 2011 M_w 9.0 earthquake. The cumulative stress fields 3 months before (left column) and after (right column) the mainshocks are presented. The mainshock locations and calculation periods are denoted. The mainshocks primarily occurred in the regions around high stress gradients.

The 1960 M_w 9.5 earthquake and the 2010 M_w 8.8 earthquake occurred in this trench. Sixteen earthquakes with moment magnitudes $M \geq 8.0$ occurred in 1900–2020. These great earthquakes generally occurred at latitudes between -40° and -10° along the subduction zones. The largest earthquake in 1900–2020, with moment magnitude of M_w 9.5, occurred in 1960 in this region. Localized high cumulative Coulomb stress changes are observed around the subduction zone at latitudes of -18° , -23° , and -38° (U1-A, U1-B, and U1-C in Figure 19). The levels of induced stresses reach 333.7 bar. We observe high lateral stress contrasts in the trench-parallel directions around the seismic gaps.

9.2. Zone 2

A large number of earthquakes occurred along the Middle America Trench where the Cocos plate is convergent with the Caribbean plate and North American plate (Figure 20). The dipping angle of subduction plate in the Middle America Trench is 18° – 32° up to a depth of 50 km, and increases high at deeper depths. The relative plate motions cause low-angle reverse-faulting events prevail in the plate boundary at shallow depths. The northern plate margin of the Caribbean plate displays a strike-slip motion with respect to the North American plate, which may load the stress on the Middle America Trench. A Guerrero seismic gap is located in the central Middle America Trench at latitudes of $\sim 12^\circ$ (Kostoglodov et al., 1996, 2001).

There were five earthquakes with moment magnitudes ≥ 8.0 in 1900–2020 in the region. Most large earthquakes with moment magnitudes ≥ 7.0 occur along the Middle America plate. The large earthquakes produced heterogeneous stress fields over the subduction zone. The 2017 M_w 8.2 earthquake loaded the

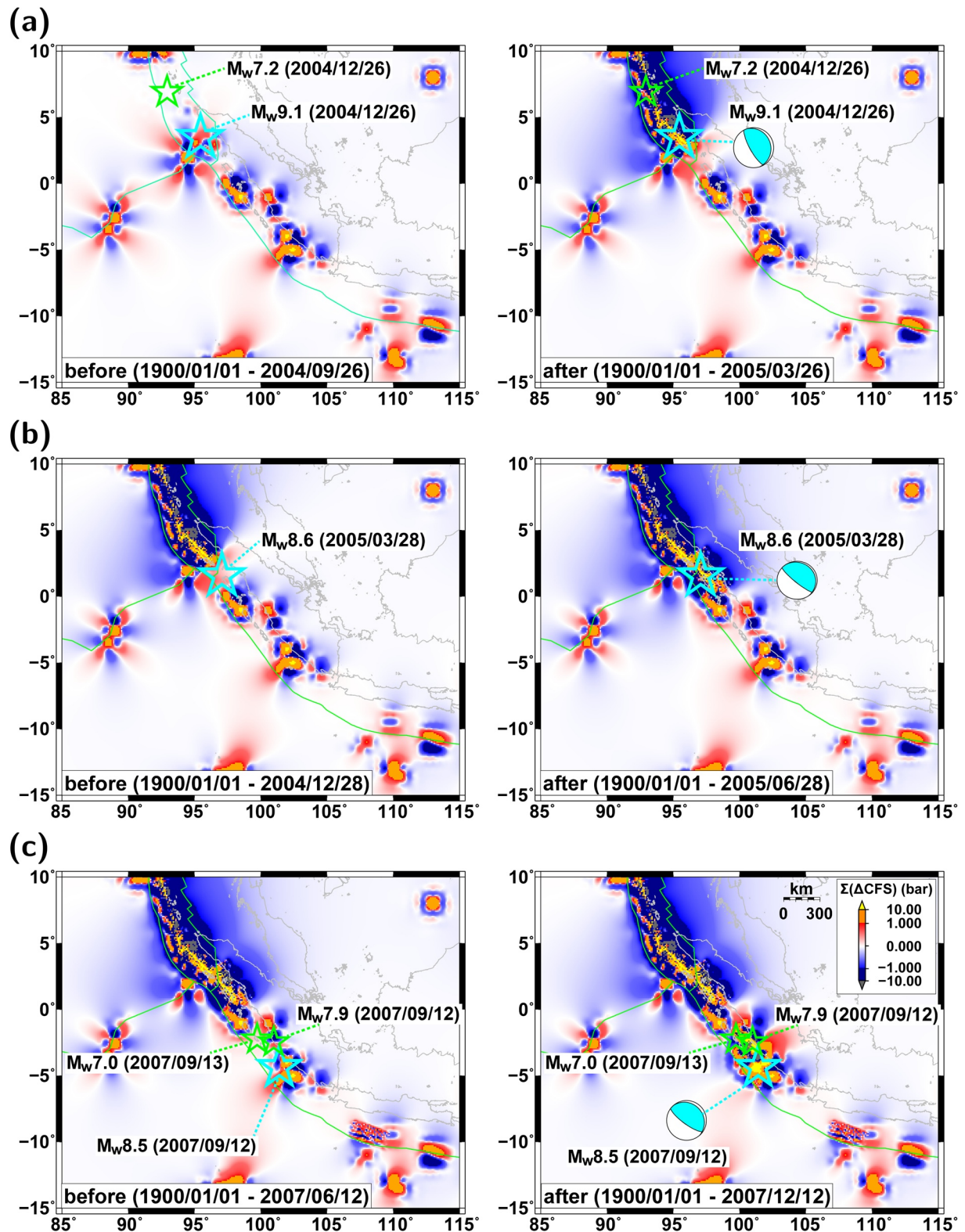


Figure 16. Temporal evolution of cumulative changes of Coulomb stress changes for optimally oriented reverse faults around the Java Trench before and after (a) the December 26, 2004 $M_w 9.1$ earthquake, (b) the March 28, 2005 $M_w 8.6$ earthquake, and (c) the September 12, 2007 $M_w 8.5$ earthquake. The cumulative stress fields before (left column) and after (right column) the mainshocks are presented. The mainshock locations and calculation periods are denoted. The mainshocks primarily occurred in the regions around high stress gradients.

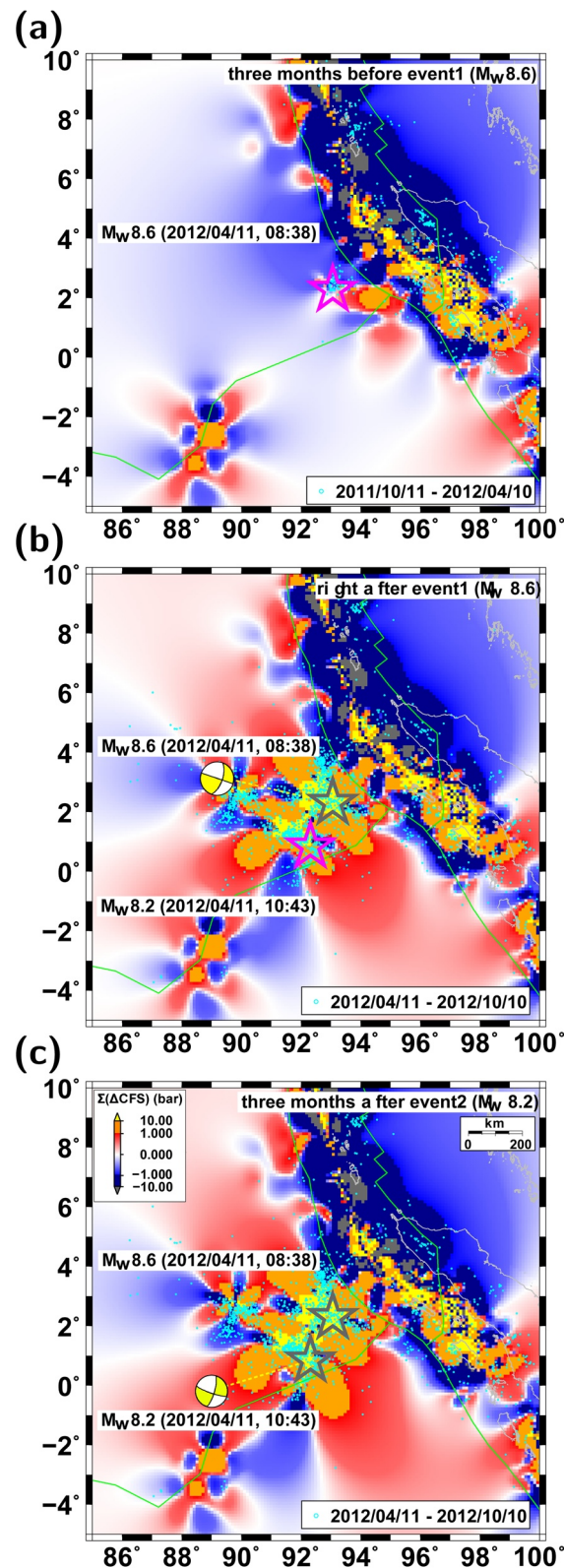


Figure 17. Temporal evolution of cumulative Coulomb stress changes for optimally oriented strike-slip faults in the northern Sumatra region: Cumulative Coulomb stress changes (a) before and (b) after the April 11, 2012 M_w 8.6 earthquake (first event), and (c) after the April 11, 2012 M_w 8.2 earthquake (second event). The second event (M_w 8.2) occurred within 2 h after the first event (M_w 8.6). The seismicity is denoted by dots. The seismicity increased in the regions of positive Coulomb stress changes.

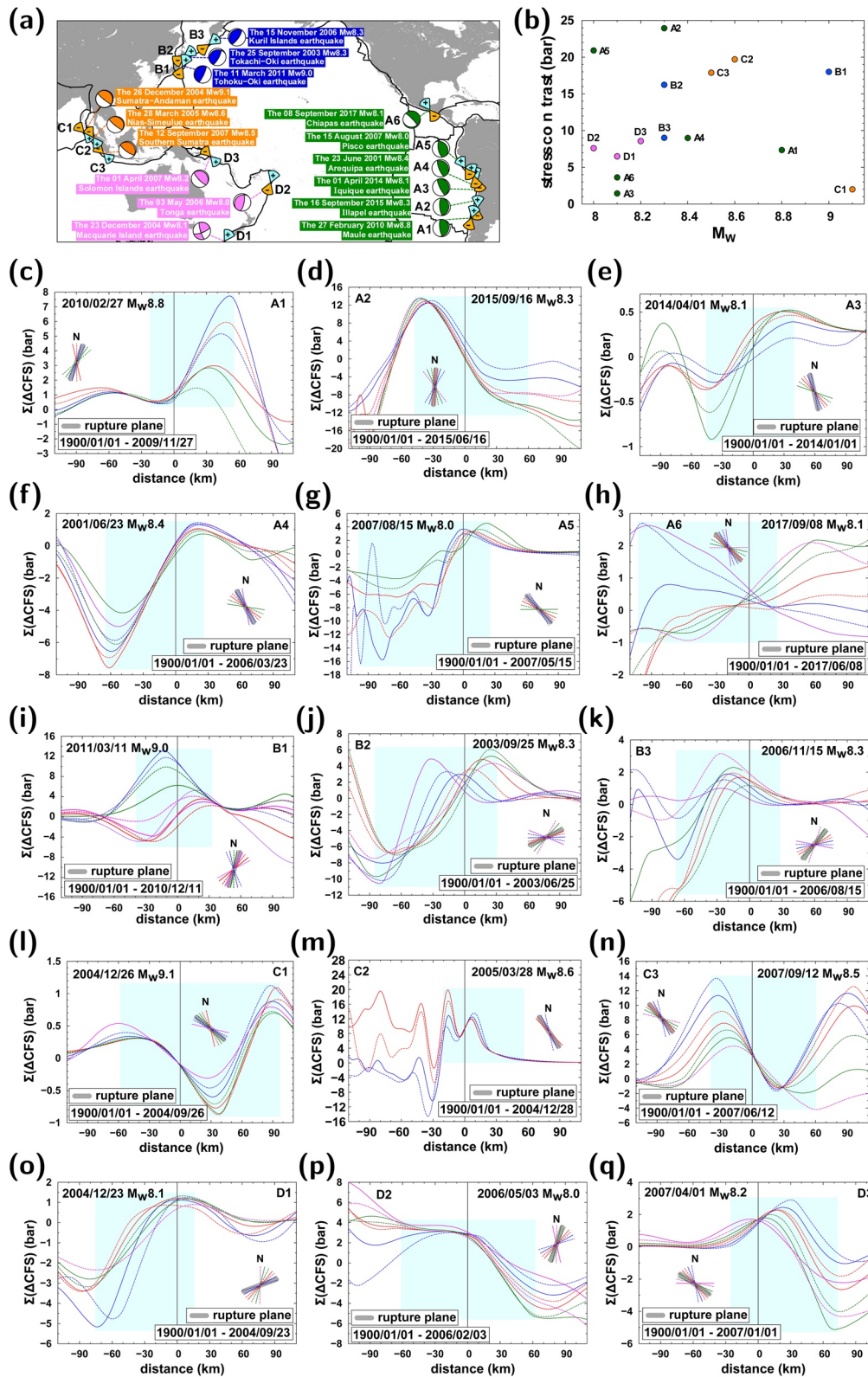


Figure 18.

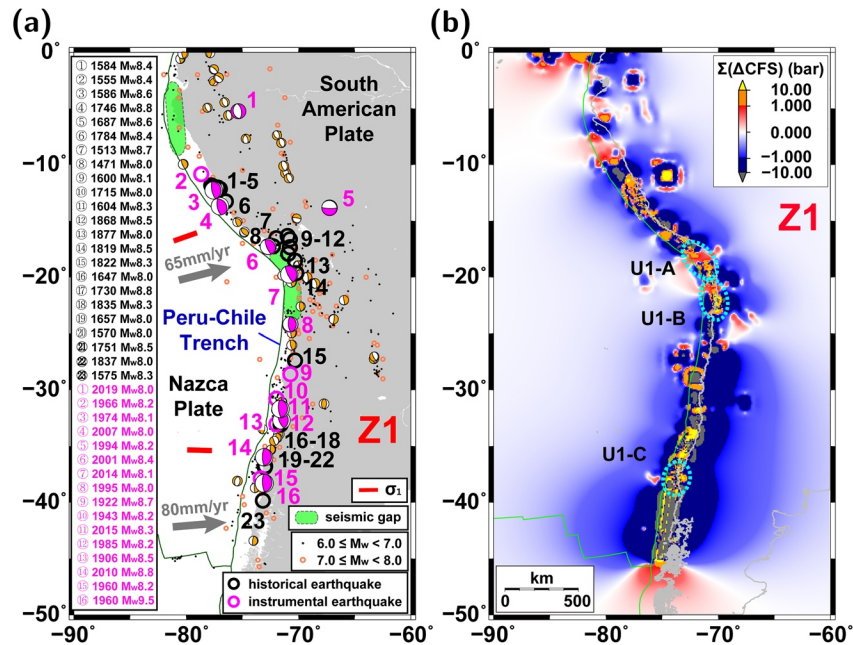


Figure 19. Cumulative Coulomb stress changes around the Peru-Chile Trench (zone 1) for optimally oriented reverse faults in 1900–2020: (a) map of major earthquakes and (b) induced stress fields. Major instrumental (black circles) earthquakes and historically large earthquakes (magenta circles) are presented.

stress around the source region. No earthquake with moment magnitude greater than 8.0 has occurred in the Guerrero seismic gap since the 1845 M_w 8.3 earthquake. We observe large lateral stress contrasts in trench-parallel directions at both ends of the Guerrero seismic gap (Figure 20).

9.3. Zone 3

The Pacific plate presents strike-slip motions with respect to the North American plate (Figure 21). Strike-slip earthquakes are dominant along the plate boundary. The Juan de Fuca plate subducts beneath the North American plate. Moderate-size reverse-faulting earthquakes occur in the Cascadia subduction zone between North American plate and Juan de Fuca plate. Most earthquakes with moment magnitudes ≥ 7.0 occur along the boundaries between the Pacific plate and the North American plate. Strike-slip events occur dominantly along the plate boundary.

Some strike-slip events occur along the transform faults between the Juan de Fuca plate and the Pacific plate. We add 13 earthquakes with moment magnitudes greater than or equal to M_w 6.4 since 1976 for calculation of induced stress fields around the Juan de Fuca plate. The stress induced by the large earthquakes is dominant along the boundary between the Pacific plate and the North American plate, where reverse faults are not present (Figure 21).

Figure 18. Lateral variation in cumulative Coulomb stress changes 3 months before great earthquakes. (a) Map of 15 earthquakes with magnitudes ≥ 8.0 since 2000, (b) summary plot of peak-to-peak cumulative Coulomb stress changes in the source regions of the earthquakes, and directional cumulative Coulomb stress change variations of each event: (c) the February 27, 2010 M_w 8.8 Maule earthquake (event A1), (d) the September 16, 2015 M_w 8.3 Illapel earthquake (event A2), (e) the April 1, 2014 M_w 8.1 Iquique earthquake (event A3), (f) the June 23, 2001 M_w 8.4 Arequipa earthquake (event A4), (g) the August 15, 2007 M_w 8.0 Pisco earthquake (event A5), (h) the September 8, 2017 M_w 8.1 Chiapas earthquake (event A6), (i) the March 11, 2011 M_w 9.0 earthquake (event B1), (j) the September 25, 2003 M_w 8.3 earthquake (event B2), (k) the November 15, 2006 M_w 8.3 Kuril Islands earthquake (event B3), (l) the December 26, 2004 M_w 9.1 Sumatra-Andaman earthquake (event C1), (m) the March 28, 2005 M_w 8.6 Nias-Simeulue earthquake (event C2), (n) the September 12, 2007 M_w 8.5 Southern Sumatra earthquake (event C3), (o) the December 23, 2004 M_w 8.1 Macquarie Island earthquake (event D1), (p) the May 3, 2006 M_w 8.0 Tonga earthquake (event D2), and (q) the April 1, 2007 M_w 8.2 Solomon Islands earthquake (event D3). The cross section lines of induced stress fields are indicated on the map and diagrams. The large earthquakes occurred in the regions with high gradients in induced stress fields. The stress contrasts presented in the summary plot are measured for the shaded ranges in the directional cumulative Coulomb stress change variations.

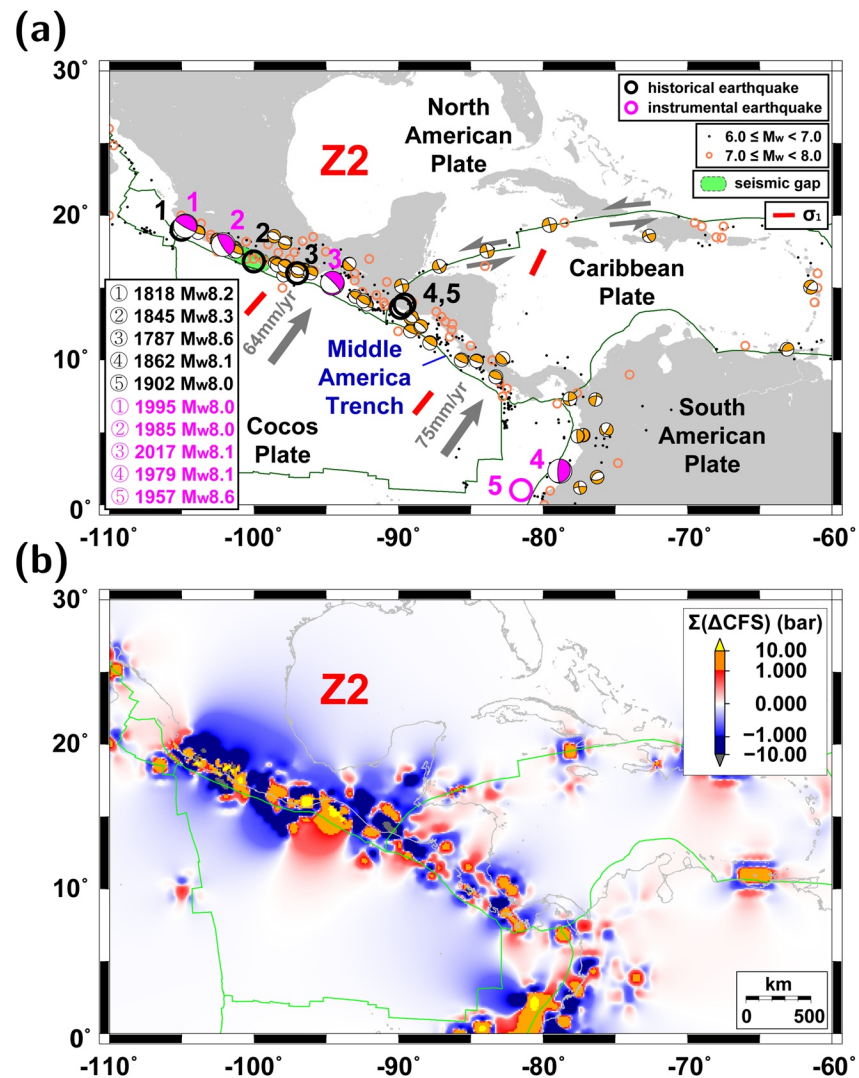


Figure 20. Cumulative Coulomb stress changes around the Middle America Trench (zone 2) for optimally oriented reverse faults in 1900–2020: (a) map of major earthquakes and (b) induced stress field. Major instrumental (black circles) earthquakes and historical large earthquakes (magenta circles) are presented.

We calculate the cumulative Coulomb stress changes with consideration of optimally oriented strike-slip faults for the western North American plate. The seismicity is dominant at depths 4–20 km. We calculate the cumulative Coulomb stress changes for two representative depths of 10 and 30 km considering the seismogenic depths in zone 3 and the other zones (Figure 21).

We observe localized large Coulomb stress changes for optimally oriented strike-slip faults in several regions along the plate boundary at latitudes of 30°, 35°, and 40° (regions U3-A, U3-B, and U3-C in Figure 21). Stress transfers from the subduction zone to strike-slip faults are observed in the region, suggesting the interaction between thrusts in the subduction zone and intraplate strike-slip faults (J. Lin & Stein, 2004).

9.4. Zone 4

The Pacific plate collides with the North American plate in the Aleutian Trench (Figure 22). The 1964 M_w 9.2 earthquake occurred in this region. Five earthquakes with moment magnitudes ≥ 8.0 occurred since 1900. The earthquakes with moment magnitudes ≥ 7.0 are distributed homogeneously over the subduction

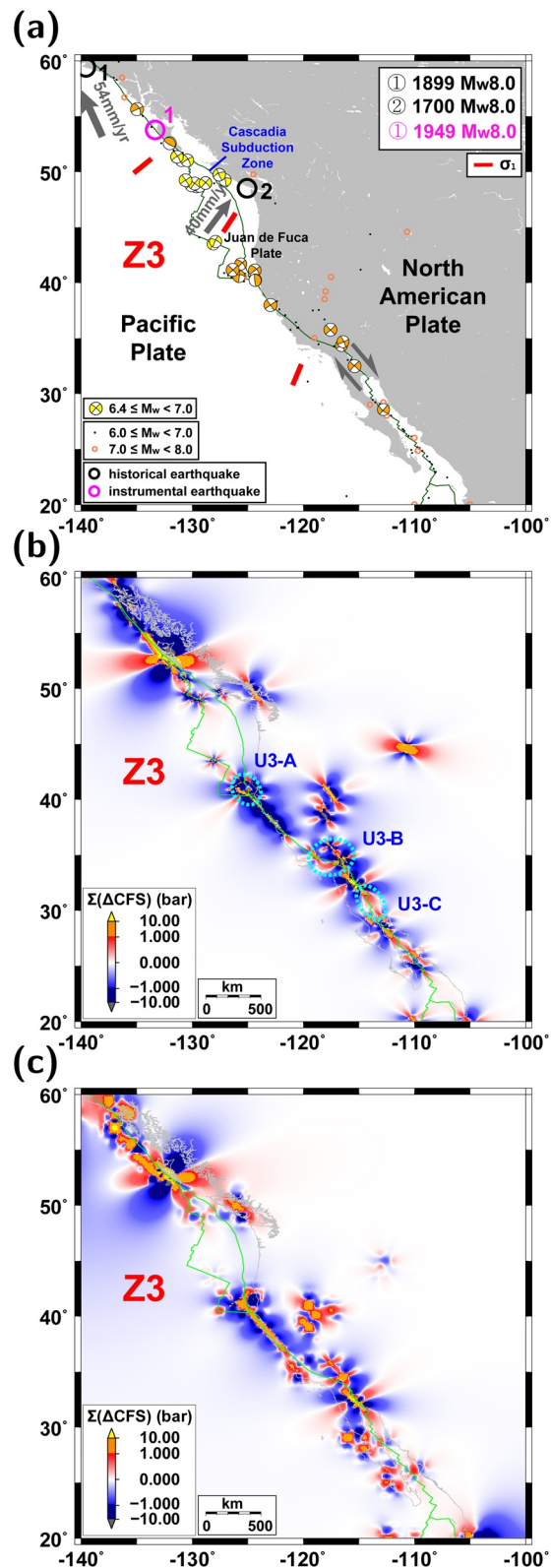


Figure 21. Cumulative Coulomb stress changes around the Cascadia Subduction Zone (zone 3) in 1900–2020: (a) map of major earthquakes, and induced stress fields for (b) optimally oriented strike-slip faults at depths of (b) 10 km and (c) 30 km. Major instrumental (black circles) earthquakes and historical large earthquakes (magenta circles) are presented.

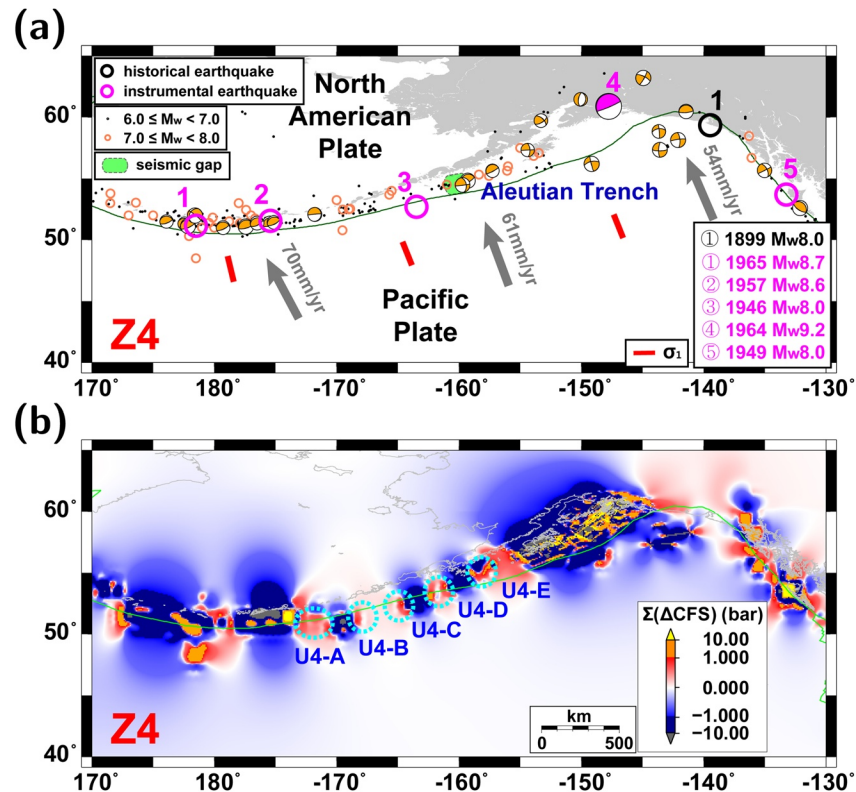


Figure 22. Cumulative Coulomb stress changes around the Aleutian Trench (zone 4) for optimally oriented reverse faults in 1900–2020: (a) map of major earthquakes and (b) induced stress fields. Major instrumental (black circles) earthquakes and historically large earthquakes (magenta circles) are presented.

zone. Strong negative Coulomb stress changes are observed in the source region of the 1964 M_w 9.2 earthquake (Wei et al., 2012).

We find regions of localized stress contrasts along the subduction zones, including the locations at longitudes of -172° , -168° , -165° , -162° , and -158° (U4-A, U4-B, U4-C, U4-D, and U4-E in Figure 22). In particular, we observed high stress induction at the western and eastern margins of the 1964 M_w 9.2 earthquake source zone. The Shumagin seismic gap is located in the eastern Aleutian Trench at longitude of -161° (J. Davies et al., 1981; Wyss & Wiemer, 1999). The Shumagin seismic gap is within the stress shadow. We find high induced stresses at both ends of the seismic gap (Figure 22).

9.5. Zone 5

The Pacific plate and Philippine Sea plate collide with the Okhotsk plate and Eurasian plate around the east coast of the Japanese islands (Figure 23). There have been many earthquakes along the subduction zones off the Japanese islands. Twenty one earthquakes with moment magnitudes ≥ 8.0 occurred along the subduction zones including the Kuril Trench, Japan Trench, Nankai Trough, and Ryukyu Trench since 1900. Large earthquakes over the previous 100 years lowered the stress levels over most regions along the Japan Trench and Nankai Trough. There are seismic gaps in the eastern Nankai Trough, northern Kuril Trench, and western Aleutian Trench, such as the Commander gap and Tokai gap (Chebrov et al., 2019; Geller, 2011; MacInnes et al., 2016) (Figure 23).

The September 25, 2003 M_w 8.3 earthquake and the March 11, 2011 M_w 9.0 earthquake relieved strong stress contrasts in the Japan Trench. We, however, observe elevated stresses in the Tokai region of Nankai Trough, where large slip deficits are present (Hok et al., 2011). We find a localized stress increase in regions around latitudes of 152° , 159° , and 165° in the Kuril Trench (U5-A, U5-B, and U5-C in Figure 23). We observe increased cumulative stress in the western Aleutian Trench. Additionally, Coulomb stress increases are

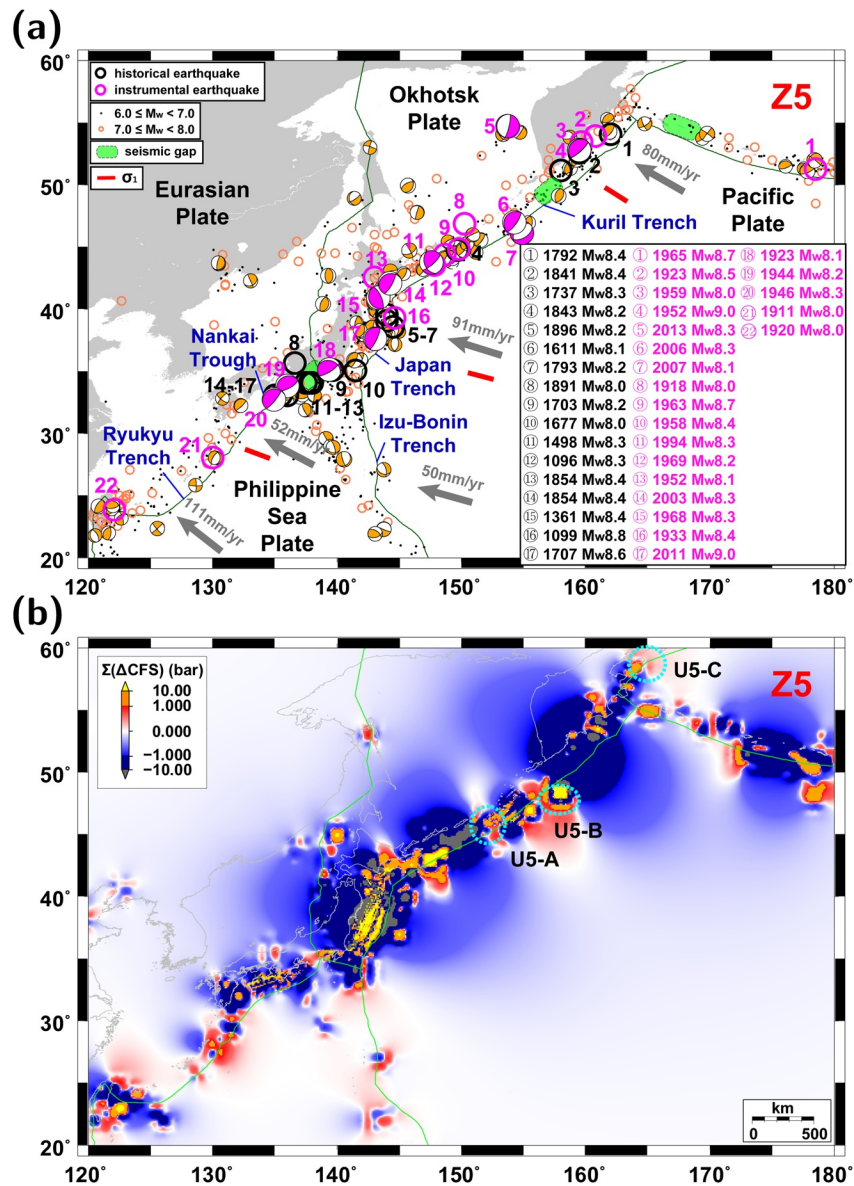


Figure 23. Cumulative Coulomb stress changes around the Kuril, Japan, and Ryukyu Trenches (zone 5) for optimally oriented reverse faults in 1900–2020: (a) map of major earthquakes and (b) induced stress fields. Major instrumental (black circles) earthquakes and historically large earthquakes (magenta circles) are presented.

observed in wide regions over the Ryukyu and Mariana Trenches, thus constructing weak lateral stress contrasts (Figure 23).

9.6. Zone 6

The Philippine Sea plate collides with the northwestern Eurasian plate at the Ryukyu Trench, and with the western Sunda plate at the Philippine Trench. The Pacific plate subducts beneath the Philippine Sea plate in the Mariana Trench (Figure 24). Fifteen earthquakes with moment magnitudes ≥ 8.0 occurred in the subduction zones since 1900. There is a central seismic gap at the latitude of $\sim 15^\circ$ (Ramos et al., 2005).

Large earthquakes produced large lateral perturbation in stress fields around the margins of the Philippine Sea plate (Figure 24). We observe large stress contrasts for a few earthquakes in a region of latitudes

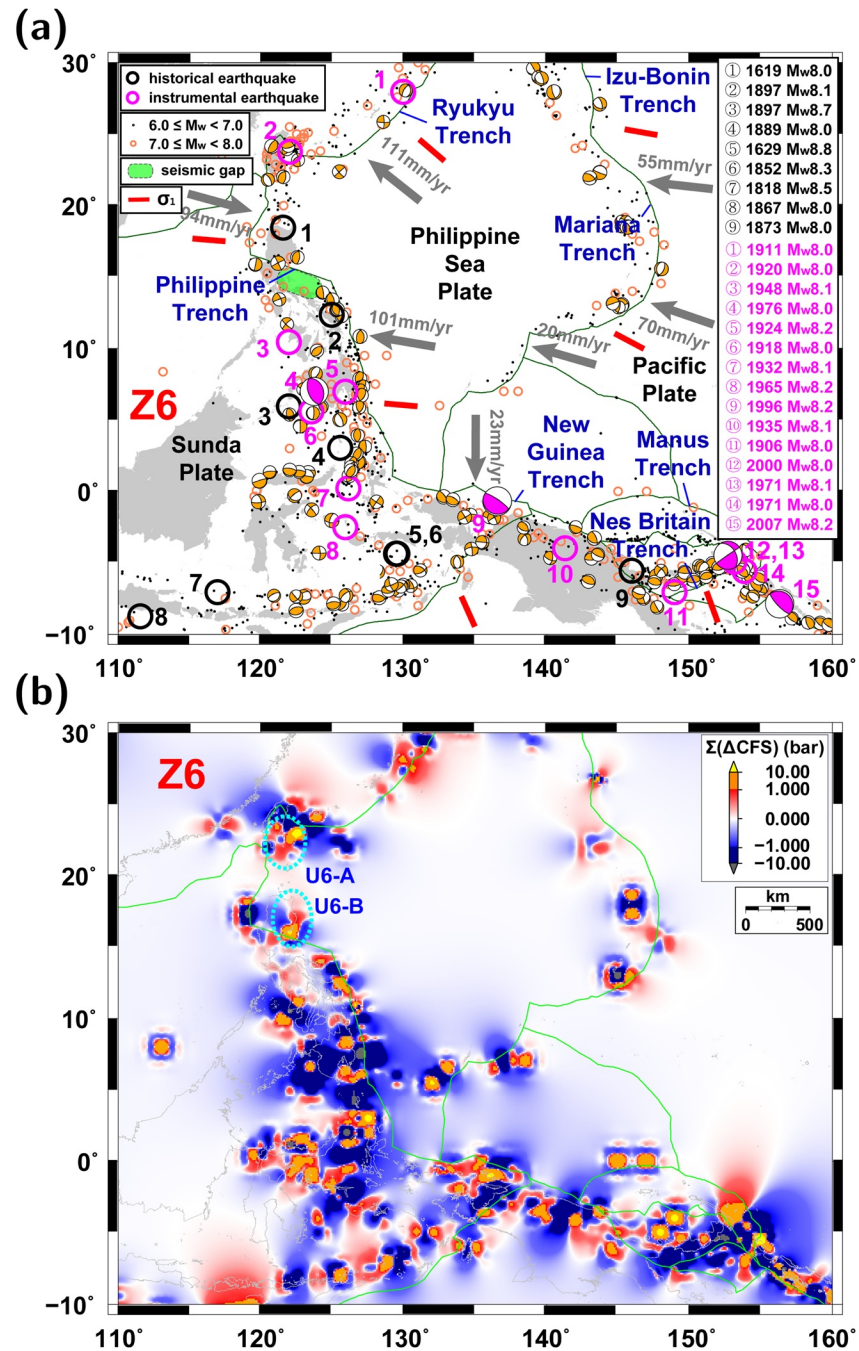


Figure 24. Cumulative Coulomb stress changes around the Izu-Bonin, Mariana, and Philippine Trenches (zone 6) for optimally oriented reverse faults in 1900–2020: (a) map of major earthquakes and (b) induced stress fields. Major instrumental (black circles) earthquakes and historically large earthquakes (magenta circles) are presented.

between 15° and 23° (U6-A and U6-B in Figure 24). The cumulative Coulomb stress changes vary smoothly in the northern Mariana Trench (Figure 24).

9.7. Zone 7

Large earthquakes occurred frequently around the Tonga Trench, New Hebrides Trench, South Solomon Trench, and New Britain Trench (Figure 25). Seventeen earthquakes with moment magnitudes ≥8.0

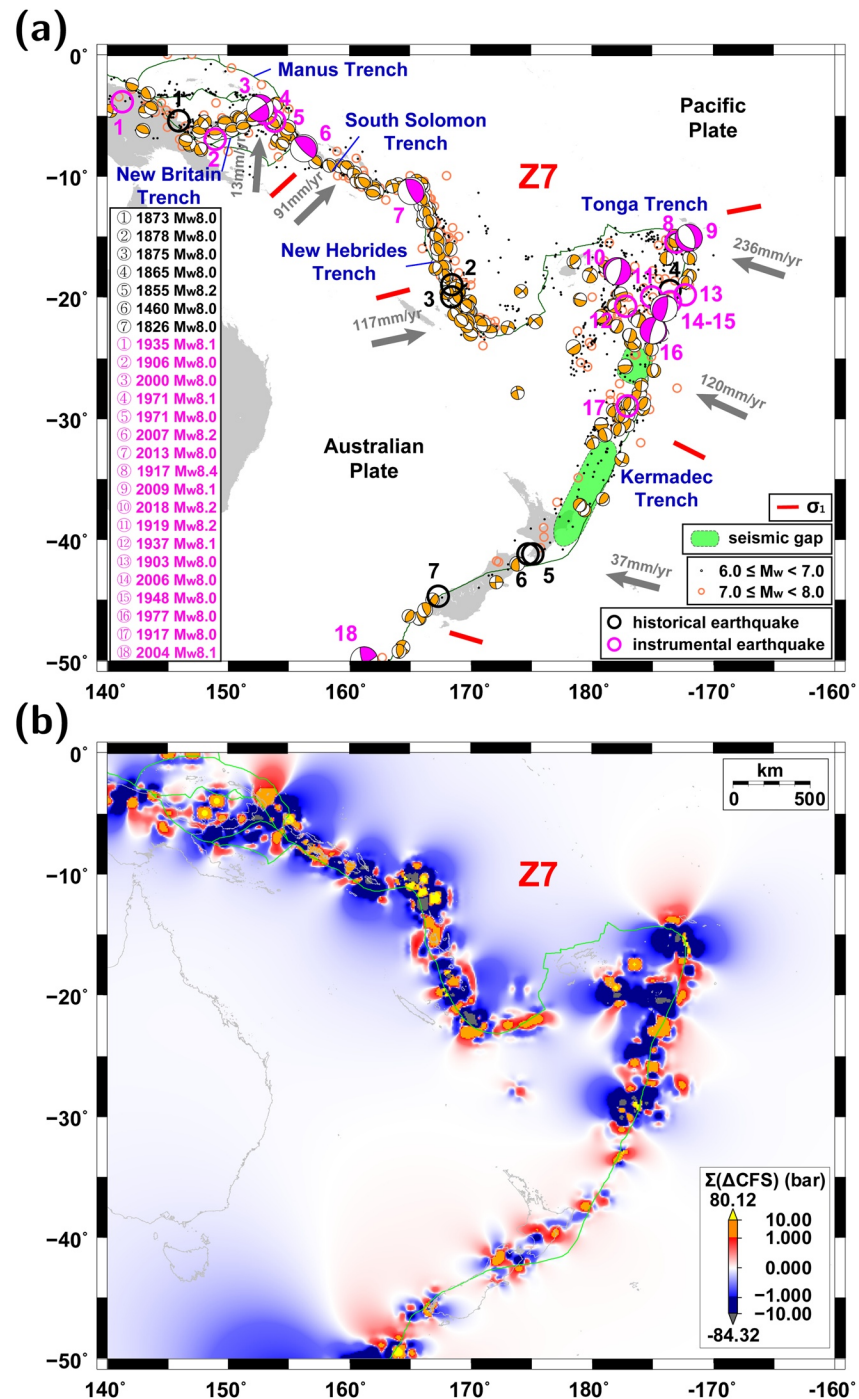


Figure 25. Cumulative Coulomb stress changes around the South Solomon, New Hebrides, Tonga, and Kermadec Trenches (zone 7) for optimally oriented reverse faults in 1900–2020: (a) map of major earthquakes and (b) induced stress fields. Major instrumental (black circles) earthquakes and historically large earthquakes (magenta circles) are presented.

occurred along the plate boundaries in 1900–2020. There are seismic gaps in the central and northern Kermadec Trench in the latitudes between -42° and -32° and between -26° and -24° (Bonnardot et al., 2007) (Figure 25).

The source mechanisms are complex in the Tonga Trench. The earthquakes produced complex lateral perturbations in the stress field (Figure 25). We observe high stress contrasts in the South Solomon Trench,

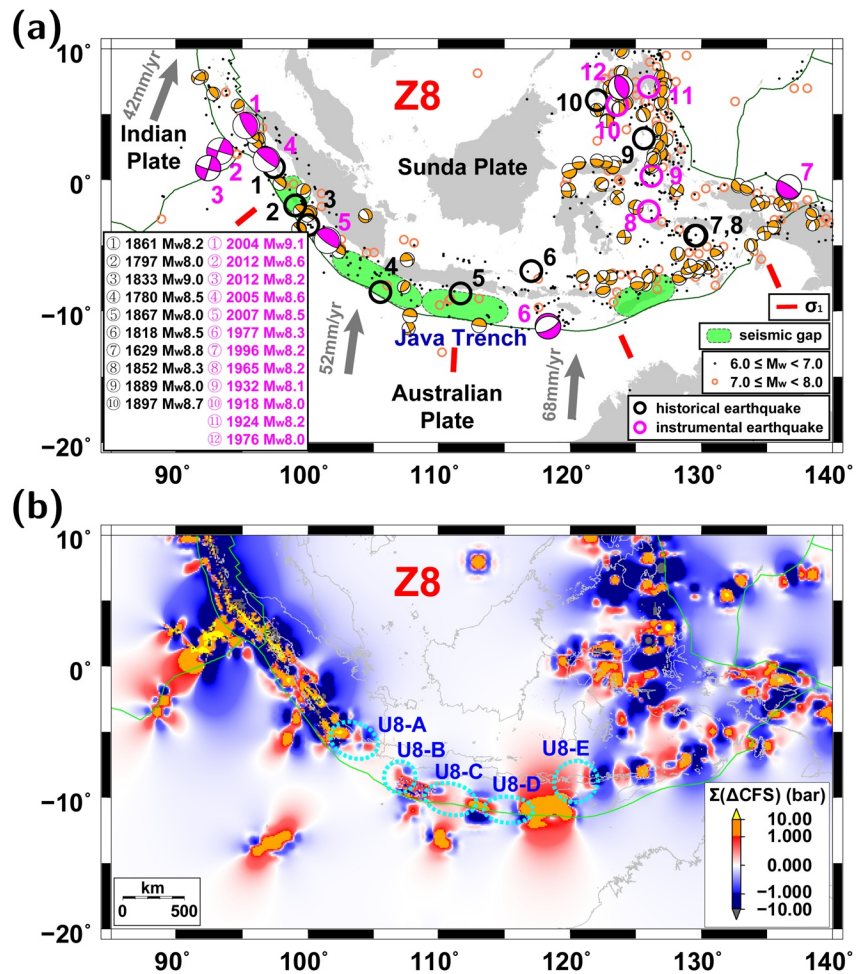


Figure 26. Cumulative Coulomb stress changes around the Java Trench (zone 8) for optimally oriented reverse faults in 1900–2020: (a) map of major earthquakes and (b) induced stress fields. Major instrumental (black circles) earthquakes and historically large earthquakes (magenta circles) are presented.

New Hebrides Trench, and Kermadec Trench. We observe strong lateral heterogeneities in the induced stress field in the seismic gap of the northern Kermadec Trench.

9.8. Zone 8

Large earthquakes occurred frequently along the Java and Philippine Trenches (Figure 26). Reverse-faulting earthquakes occur in the subduction zones. There are seismic gaps along the Java Trench (Ely & Sandiford, 2010; Mignan et al., 2006; Philiposian et al., 2017). Twelve earthquakes with moment magnitudes ≥ 8.0 occurred along the subduction zones in 1900–2020. The 2004 M_w 9.1 Sumatra-Andaman earthquake lowered the static stress level in the epicenter region, while increasing the static stress level in a region of the Java Trench, where a M_w 8.6 event occurred 3 months later. A M_w 8.5 event occurred ~ 30 months later in a region to the southeast, where the stress level was elevated.

Large strike-slip events occur in the outer rise in the Java Trench near Sumatra. Two large strike-slip earthquakes with moment magnitudes of M_w 8.6 and M_w 8.2 consecutively occurred in April 11, 2012. The M_w 8.6 strike-slip event triggered earthquakes globally (Pollitz et al., 2012). The December 26, 2004 M_w 9.1 earthquake, the March 28, 2005 M_w 8.6 earthquake, and the September 12, 2007 M_w 8.5 earthquakes in the subduction zone caused local stress perturbation with stress contrasts of 9.75 bar in the source region

of the April 11, 2012 M_w 8.6 earthquake (Figure 17). The April 11, 2012 M_w 8.6 strike-slip earthquake occurred at a region of large gradient in cumulative stress field (large stress contrast). Thus, the occurrence of the M_w 8.6 strike-slip event may be a consequence of regional stress field perturbation after consecutive great earthquakes in the subduction zone. This feature supports the stress transfer and interaction between interplate and intraplate regions among different types of faults (Ammon et al., 2008; ten Brink & Lin, 2004).

The two consecutive large strike-slip earthquakes with moment magnitudes of M_w 8.6 and M_w 8.2 occurred in a region of large stress contrast between positive and negative Coulomb stress changes (Figure 17). The two large strike-slip earthquakes loaded the stress around the epicentral region. A large number of earthquakes followed the great strike-slip events. The spatial distribution of earthquakes is correlated with the Coulomb stress changes. The two large strike-slip events significantly perturbed the stress field, accompanying successive aftershocks (Figure 17). We find localized concentration of high Coulomb stress changes along the southern Java Trench at longitudes between 102° and 122° (U8-A, U8-B, U8-C, U8-D, and U8-E in Figure 26).

10. Discussion and Conclusions

The occurrence of great earthquakes may be dependent on various parameters including slab geometry, thermal parameters, sediment thickness, strain rate, pore pressure, asperity, and slow slips (Araki et al., 2017; Chapman & Melbourne, 2009; Hippen & Hyndman, 2008; Keiding et al., 2009; Perfettini & Avouac, 2004; Saffer et al., 2000; Schwartz & Rokosky, 2007; Townend & Zoback, 2006; Uchida et al., 2016; R. E. Wells & Blakely, 2003; Yokota et al., 2016). The stress field, which controls the timing of earthquake occurrence, is not stationary.

We investigated the cumulative Coulomb stress changes at a depth of 30 km for optimally oriented reverse faults induced by earthquakes with moment magnitudes ≥ 7.0 since 1900. The considered depth is a representative depth of large earthquakes in convergent plate boundaries. For the western North American plate region (zone 3), we assessed the cumulative Coulomb stress changes at depths of 10 and 30 km for optimally oriented strike-slip faults considering the plate boundary environment and seismicity features.

We assessed the cumulative amount of induced stress fields without consideration of stress recovery with time. The analysis did not include the stress field changes induced by postseismic slips, viscoelastic medium responses, and slow slips, which may be critical for the stress field. We investigated possible effects of induced stress on the occurrence of next earthquakes.

We have 120-year-long instrumentally recorded earthquake. We assess the amounts of stress induced by precedent earthquakes for 120 years. The presented cumulative stress changes represent the component of coseismic stress transfer from neighboring earthquakes. The analysis is useful to quantify the upper and lower bounds of induced stresses from neighboring earthquakes. Also, this study provides a reference to examine the influence of induced stress on seismicity.

We observed complex induced stress fields over plate boundaries. Large earthquakes dominantly perturbed the stress fields around plate boundaries. The cumulative Coulomb stress changes changed with time, evolving in complex appearance. We observed laterally heterogeneous stress fields along most plate boundaries. The stress contrasts varied from tens to hundreds of bar. The tectonic-loading stress may be the primary source of the static stress field that is spatially homogeneous and continuous. We observed that the cumulative stresses induced by precedent earthquakes are spatially inhomogeneous and localized. The magnitudes of tectonic-loading stresses are hundreds of times larger than those of induced stresses (Kato, 2012; King et al., 1994; Lamb, 2005; Toda et al., 2012; Yagi & Fukahata, 2011).

The coseismic stress decreases are on the order of tens to hundreds of bar (Hasegawa, 2017; Stein et al., 1997), nearly equivalent to the levels of peak cumulative induced stresses. This observation suggests that the stress induced from neighboring earthquakes for 120 years is sufficient for recovery of coseismic stress decreases. The induced stress constructs a laterally heterogeneous stress field.

Great earthquakes occurred in regions with large lateral variations in Coulomb stress changes. The regions display stress contrasts of 2.5–30 bar. Additionally, the epicenters of great earthquakes such as the 2003 M_w 8.3 Tokachi-Oki earthquake, the 2011 M_w 9.0 Tohoku-Oki earthquake, and the 2010 M_w 8.8 Maule earthquake generally correspond to the regions of large slip deficits (Hashimoto et al., 2009; Moreno et al., 2010; Suwa et al., 2006). Thus, laterally heterogeneous stress transfer triggers the earthquakes in regions of high static stress. This feature agrees with laboratory experiments (Langenbruch & Shapiro, 2015; Okazaki & Hirth, 2016). The observation suggests that the laterally heterogeneous stress field causes instability to induce earthquake occurrence. As the magnitudes of lateral perturbations increase, the instability may increase. Thus, the earthquake occurrence may be highly affected by the heterogeneity in stress field.

It is known that earthquakes can be induced at stress-increase regions (King et al., 1994; Nalbant et al., 1998; Stein et al., 1997; Toda et al., 2005). Also, long-term accumulation of induced stress may cause earthquake occurrence, which is particularly effective in regions of laterally heterogeneous stress fields. High accumulation of stress may pertain to high probability of earthquake occurrence. The high stress accumulation can be similarly achieved by a situation in which neighboring regions have relatively low stress levels.

In this study, it is not argued the induced stress from precedent earthquakes is the only controlling factor to produce earthquakes. We rather suggest that the earthquake occurrence can be fostered by stress perturbation from precedent earthquakes. We observed that stress-contrast regions may be subject to accommodate large earthquakes. This study suggests that the stress field induced from precedent earthquakes may be linked with large earthquakes.

We observed large stress contrasts at some interseismic locking zones with large slip deficits, including the northern and central Peru-Chile Trench in zone 1 around (78°W, 12°S), (75°W, 15°S), and (71°W, 21°S), Middle America Trench in zone 2 around (97°W, 16°S), (99°W, 17°S), and (101°W, 18°S), Aleutian Trench in zone 4 around (155°W, 56°N), (164°W, 52°N), (178°W, 52°N), (172.5°E, 52.5°N), Nankai Trough, Japan Trench, and Kuril Trench in zone 5 around (133°E, 32.5°N), (135.5°E, 33°N), (143°E, 41°N), and (146°E, 43°N), Ryukyu Trench in zone 6 around (130°E, 27.5°N), and (124°E, 24°N), New Hebrides Trench, and Kermadec Trench in zone 7 around (167°E, 15°S), (174°W, 22°S), and (178°E, 39°S), Java Trench in zone 8 around (103°E, 6°S) and (113°E, 10°S).

The spatiotemporal distributions of the stress fields may control the occurrence of great earthquakes. The occurrence timing of large earthquakes may be dependent on medium conditions as well as static stress level and induced stress changes. The potential locations of large earthquakes can be determined from the lateral variations of the stress field. The 120-year-long induced stress may provide a reference to identify the potential locations of ensuing large earthquakes. Further, composite analysis of seismic gaps and lateral stress-field variations may suggest the potential locations of large earthquakes.

Data Availability Statement

The data and results of this study are available on Dryad (<https://doi.org/10.5061/dryad.zkh1893b1>).

Acknowledgments

The authors thank Drs. Maureen Long (editor), Chung-Han Chan (reviewer), and an anonymous reviewer for constructive review comments. This work was supported by the Korea Meteorological Administration Research and Development Program under grant KMI2018-02910. Additionally, this research was partly supported by the Basic Science Research Program of National Research Foundation of Korea (NRF-2017R1A6A1A07015374, NRF-2018R1D1A1A09083446).

References

- Albini, P., Musson, R. M. W., Gomez Capera, A. A., Locati, M., Rovida, A., Stucchi, M., & Viganò, D. (2014). *Global historical earthquake archive and catalogue 1000-1903*. Pavia.
- Albini, P., Musson, R. M. W., Rovida, A., Locati, M., Gomez Capera, A. A., & Viganò, D. (2014). The global earthquake history. *Earthquake Spectra*, 30(2), 607–624. <https://doi.org/10.1193/122013eqs297>
- Ammon, C. J., Chen, J., Thio, H.-K., Robinson, D., Ni, S., Hjørleifsdóttir, V., et al. (2005). Rupture process of the great 2004 Sumatra-Andaman earthquake. *Science*, 308(1), 133–139. <https://doi.org/10.1126/science.1112260>
- Ammon, C. J., Kanamori, H., & Lay, T. (2008). A great earthquake doublet and seismic stress transfer cycle in the central Kuril Islands. *Nature*, 451, 561–565. <https://doi.org/10.1038/nature06521>
- Araki, E., Saffer, D. M., Kopf, A. J., Wallace, L. M., Kimura, T., Machida, Y., et al. (2017). Recurring and triggered slow-slip events near the trench at the Nankai Trough subduction megathrust. *Science*, 356(1), 1157–1160. <https://doi.org/10.1126/science.aan3120>
- Asano, K., Iwata, T., & Irikura, K. (2005). Estimation of source rupture process and strong ground motion simulation of the 2002 Denali, Alaska, earthquake. *Bulletin of the Seismological Society of America*, 95(5), 1701–1715. <https://doi.org/10.1785/0120040154>

- Audet, P., & Kim, Y. (2016). Teleseismic constraints on the geological environment of deep episodic slow earthquakes in subduction zone forearcs: A review. *Tectonophysics*, *670*, 1–15. <https://doi.org/10.1016/j.tecto.2016.01.005>
- Baba, Y., Tanioka, Y., Cummins, P. R., & Uhira, K. (2002). The slip distribution of the 1946 Nankai earthquake estimated from tsunami inversion using a new plate model. *Physics of the Earth and Planetary Interiors*, *132*(1–3), 59–73. [https://doi.org/10.1016/S0031-9201\(02\)00044-4](https://doi.org/10.1016/S0031-9201(02)00044-4)
- Beck, S. L., Barrientos, S., Kausel, E., & Reyes, M. (1998). Source characteristics of historic earthquakes along the central Chile subduction zone. *Journal of South American Earth Sciences*, *11*(2), 115–129. [https://doi.org/10.1016/S0895-9811\(98\)00005-4](https://doi.org/10.1016/S0895-9811(98)00005-4)
- Beck, S. L., & Christensen, D. H. (1991). Rupture process of the February 4, 1965, Rat Islands earthquake. *Journal of Geophysical Research*, *96*(B2), 2205–2221. <https://doi.org/10.1029/90jb02092>
- Bird, P. (2003). An updated digital model of plate boundaries. *Geochemistry, Geophysics, Geosystems*, *4*(3), 1027. <https://doi.org/10.1029/2001GC0025210.1029/2001gc000252>
- Blaser, L., Krüger, F., Ohrnberger, M., & Scherbaum, F. (2010). Scaling relations of earthquake source parameter estimates with special focus on subduction environment. *Bulletin of the Seismological Society of America*, *100*(6), 2914–2926. <https://doi.org/10.1785/0120100111>
- Bonnardot, M. A., Régnier, M., Ruellan, E., Christova, C., & Tric, E. (2007). Seismicity and state of stress within the overriding plate of the Tonga-Kermadec subduction zone. *Tectonics*, *26*(5), TC5017. <https://doi.org/10.1029/2006TC002044>
- Bowman, D. D., & King, G. C. P. (2001). Accelerating seismicity and stress accumulation before large earthquakes. *Geophysical Research Letters*, *28*(21), 4039–4044. <https://doi.org/10.1029/2001gl013022>
- Boyd, T. M., Engdahl, E. R., & Spence, W. (1999). Seismic cycles along the Aleutian arc: Analysis of seismicity from 1957 through 1991. *Journal of Geophysical Research*, *100*(B1), 621–644.
- Cattin, R., Chamot-Rooke, N., Pubellier, M., Rabaute, A., Delescluse, M., Vigny, C., et al. (2009). Stress change and effective friction coefficient along the Sumatra-Andaman-Sagaing fault system after the 26 December 2004 (Mw9.2) and the 28 March 2005 (Mw8.7) earthquakes. *Geochemistry, Geophysics, Geosystems*, *10*, Q03011. <https://doi.org/10.1029/2008GC002167>
- Chan, C.-H., & Stein, R. S. (2009). Stress evolution following the 1999 Chi-Chi, Taiwan, earthquake: Consequences for afterslip, relaxation, aftershocks and departures from Omori decay. *Geophysical Journal International*, *177*, 179–192. <https://doi.org/10.1111/j.1365-246x.2008.04069.x>
- Chapman, J. S., & Melbourne, T. I. (2009). Future Cascadia megathrust rupture delineated by episodic tremor and slip. *Geophysical Research Letters*, *36*, L22301. <https://doi.org/10.1029/2009GL040465>
- Chebrov, D. V., Kugaenko, Y. A., Lander, A. V., Abubakirov, I. R., Gusev, A. A., Droznina, S. Y., et al. (2019). Near islands Aleutian earthquake with Mw 7.8 on July 17, 2017: I. Extended rupture along the Commander block of the Aleutian island arc from observations in Kamchatka, Izvestiya. *Physics of the Solid Earth*, *55*(4), 576–599. <https://doi.org/10.1134/S1069351319040037>
- Cloos, M. (1992). Thrust-type subduction-zone earthquakes and seamount asperities: A physical model for seismic rupture. *Geology*, *20*, 601–604. [https://doi.org/10.1130/0091-7613\(1992\)020<0601:tszea>2.3.co;2](https://doi.org/10.1130/0091-7613(1992)020<0601:tszea>2.3.co;2)
- Cloos, M., & Shreve, R. L. (1994). Shear-zone thickness and the seismicity of Chilean- and Mariana-type subduction zones. *Geology*, *24*, 107–110.
- Cocco, M., Nostro, C., & Ekstrom, G. (2000). Static stress changes and fault interaction during the 1997 Umbria-Marche earthquake sequence. *Journal of Seismology*, *4*, 501–516. <https://doi.org/10.1023/a:1026507917308>
- Courboulx, F., Santoyo, M. A., Pacheco, J. F., & Singh, S. K. (1997). The 14 September 1995 (M 7.3) Copala, Mexico, earthquake: A source study using teleseismic, regional, and local data. *Bulletin of the Seismological Society of America*, *87*, 999–1010.
- Currie, C. A., Hyndman, R. D., Wang, K., & Kostoglodov, V. (2002). Thermal models of the Mexico subduction zone: Implications for the megathrust seismogenic zone. *Journal of Geophysical Research*, *107*(B12). <https://doi.org/10.1029/2001JB000886>
- Davies, J. H. (2013). Global map of solid Earth surface heat flow. *Geochemistry, Geophysics, Geosystems*, *14*(10), 4608–4622. <https://doi.org/10.1002/ggge.20271>
- Davies, J., Sykes, L., House, L., & Jacob, K. (1981). Shumagin seismic gap, Alaska Peninsula: History of great earthquakes, tectonic setting, and evidence for high seismic potential. *Journal of Geophysical Research*, *86*(B5), 3821–3855. <https://doi.org/10.1029/jb086ib05p03821>
- Delouis, B., Cisternas, A., Dorbath, L., Rivera, L., & Kausel, E. (1996). The Andean subduction zone between 22 and S (northern Chile): Precise geometry and state of stress. *Tectonophysics*, *259*, 81–100. [https://doi.org/10.1016/0040-1951\(95\)00065-8](https://doi.org/10.1016/0040-1951(95)00065-8)
- Delouis, B., Pardo, M., Legrand, D., & Monfret, T. (2007). The Mw 7.7 Tocopilla earthquake of 14 November 2007 at the southern edge of the northern Chile seismic gap: Rupture in the deep part of the coupled plate interface. *Bulletin of the Seismological Society of America*, *99*(1), 87–94.
- Dixon, T. H., Jiang, Y., Malservisi, R., McCaffrey, R., Voss, N., Protti, M., & Gonzalez, V. (2014). Earthquake and tsunami forecasts: Relation of slow slip events to subsequent earthquake rupture. *Proceedings of the National Academy of Sciences of the United States of America*, *111*(48), 17039–17044. <https://doi.org/10.1073/pnas.1412299111>
- Elliott, J. R., Walters, R. J., England, P. C., Jackson, J. A., Li, Z., & Parsons, B. (2010). Extension on the Tibetan plateau: Recent normal faulting measured by InSAR and body wave seismology. *Geophysical Journal International*, *183*(2), 503–535. <https://doi.org/10.1111/j.1365-246x.2010.04754.x>
- Ely, K. S., & Sandiford, M. (2010). Seismic response to slab rupture and variation in lithospheric structure beneath the Savu Sea, Indonesia. *Tectonophysics*, *483*, 112–124. <https://doi.org/10.1016/j.tecto.2009.08.027>
- Engdahl, E. R., & Villaseñor, A. (2002). Global seismicity: 1900–1999. In W. H. K. Lee, H. Kanamori, P. C. Jennings, & C. Kisslinger (Eds.), *International handbook of earthquake and engineering seismology* (Part A, Chapter 41). Academic Press.
- Felzer, K. R., Abercrombie, R. E., & Ekstrom, G. (2004). A common origin for aftershocks, foreshocks, and multiplets. *Bulletin of the Seismological Society of America*, *94*, 88–98. <https://doi.org/10.1785/0120030069>
- Freed, A. M. (2005). Earthquake triggering by static, dynamic, and postseismic stress transfer. *Annual Review of Earth and Planetary Sciences*, *33*(1), 335–367. <https://doi.org/10.1146/annurev.earth.33.092203.122505>
- Fujii, Y., & Satake, K. (2013). Slip distribution and seismic moment of the 2010 and 1960 Chilean earthquakes inferred from tsunami waveforms and coastal geodetic data. *Pure and Applied Geophysics*, *170*(1), 1493–1509. <https://doi.org/10.1007/s00024-012-0524-2>
- Fukuyama, E., & Irikura, K. (1986). Rupture process of the 1983 Japan Sea (Akita-Oki) earthquake using a waveform inversion method. *Bulletin of the Seismological Society of America*, *76*(6), 1623–1640. <https://doi.org/10.1785/bssa0760061623>
- Fulton, P. M., & Saffer, D. M. (2009). Potential role of mantle-derived fluids in weakening the San Andreas Fault. *Journal of Geophysical Research*, *114*, B07408. <https://doi.org/10.1029/2008JB006087>
- Furukawa, Y., & Uyeda, S. (1989). Thermal state under the Tohoku Arc with consideration of crustal heat generation. *Tectonophysics*, *164*, 175–187. [https://doi.org/10.1016/0040-1951\(89\)90011-5](https://doi.org/10.1016/0040-1951(89)90011-5)

- Gao, X., & Wang, K. (2014). Strength of stick-slip and creeping subduction megathrusts from heat flow observations. *Science*, 345(6200), 1038–1041. <https://doi.org/10.1126/science.1255487>
- Gao, X., & Wang, K. (2017). Rheological separation of the megathrust seismogenic zone and episodic tremor and slip. *Nature*, 543, 416–419. <https://doi.org/10.1038/nature21389>
- Gardi, A., Lemoine, A., Madariaga, R., & Campos, J. (2006). Modeling of stress transfer in the Coquimbo region of central Chile. *Journal of Geophysical Research*, 111, B04307. <https://doi.org/10.1029/2004JB003440>
- Geller, R. (2011). Shake-up time for Japanese seismology. *Nature*, 472, 407–409. <https://doi.org/10.1038/nature10105>
- Graham, S., DeMets, C., Cabral-Cano, E., Kostoglodov, V., Rousset, B., Walpersdorf, A., et al. (2016). Slow slip history for the MEXICO subduction zone: 2005 trough 2011. *Pure and Applied Geophysics*, 173, 3445–3465. <https://doi.org/10.1007/s00024-015-1211-x>
- Green, R. G., Greenfield, T., & White, R. S. (2015). Triggered earthquakes suppressed by an evolving stress shadow from a propagating dyke. *Nature Geoscience*, 8, 629–632. <https://doi.org/10.1038/ngeo2491>
- Gudmundsson, Ó., & Sambridge, M. (1998). A regionalized upper mantle (RUM) seismic model. *Journal of Geophysical Research*, 103(B4), 7121–7136. <https://doi.org/10.1029/97jb02488>
- Han, S., Bangs, N. L., Carbotte, S. M., Saffer, D. M., & Gibson, J. C. (2017). Links between sediment consolidation and Cascadia megathrust slip behaviour. *Nature Geoscience*, 10, 954–959. <https://doi.org/10.1038/s41561-017-0007-2>
- Harris, R. A., & Simpson, R. W. (1998). Suppression of large earthquakes by stress shadows: A comparison of Coulomb and rate-and-state failure. *Journal of Geophysical Research*, 103(B10), 24439–24451. <https://doi.org/10.1029/98jb00793>
- Harris, R. N., Spinelli, G., Ranero, C. R., Grevenmeyer, I., Villinger, H., & Barckhausen, U. (2010). Thermal regime of the Costa Rican convergent margin: 2. Thermal models of the shallow Middle America subduction zone offshore Costa Rica. *Geochemistry, Geophysics, Geosystems*, 11, Q12S29. <https://doi.org/10.1029/2010GC003273>
- Harris, R. N., & Wang, K. (2002). Thermal models of the Middle America Trench at the Nicoya Peninsula, Costa Rica. *Geophysical Research Letters*, 29, 2010. <https://doi.org/10.1029/2002GL015406>
- Hartzell, S., & Langer, C. (1993). Importance of model parameterization in finite fault inversions; application to the 1974 Mw 8.0 Peru earthquake. *Journal of Geophysical Research*, 98, 22123–22134. <https://doi.org/10.1029/93jb02453>
- Hasegawa, A. (2017). Role of H₂O in generating subduction zone earthquakes. *Monographs on Environment, Earth and Planets*, 5, 1–34. <https://doi.org/10.5047/meep.2017.00501.0001>
- Hashimoto, C., Noda, A., Sagiya, T., & Matsu'ura, M. (2009). Interplate seismogenic zones along the Kuril-Japan trench inferred from GPS data inversion. *Nature Geoscience*, 2, 141–144. <https://doi.org/10.1038/ngeo421>
- Hayes, G. P. (2017). The finite, kinematic rupture properties of great-sized earthquakes since 1990. *Earth and Planetary Science Letters*, 468, 94–100. <https://doi.org/10.1016/j.epsl.2017.04.003>
- Hayes, G. P., Herman, M. W., Barnhart, W. D., Furlong, K. P., Riquelme, S., Benz, H. M., et al. (2014). Continuing megathrust earthquake potential in Chile after the 2014 Iquique earthquake. *Nature*, 512, 295–298. <https://doi.org/10.1038/nature13677>
- Helmstetter, A., & Shaw, B. E. (2006). Relation between stress heterogeneity and aftershock rate in the rate-and-state model. *Journal of Geophysical Research*, 111, B07304. <https://doi.org/10.1029/2005JB004077>
- Helmstetter, A., & Shaw, B. E. (2009). Afterslip and aftershocks in the rate-and-state friction law. *Journal of Geophysical Research*, 114, B01308. <https://doi.org/10.1029/2007JB005077>
- Hernandez, B., Shapiro, N. M., Singh, S. K., Pacheco, J. F., Cotton, F., Campillo, M., et al. (2001). Rupture history of September 30, 1999 intraplate earthquake of Oaxaca, Mexico (Mw 7.5) from inversion of strong-motion data. *Geophysical Research Letters*, 28(2), 363–366. <https://doi.org/10.1029/2000gl011975>
- Hicks, S. P., Rietbrock, A., Haberland, C. A., Ryder, I. M. A., Simons, M., & Tassara, A. (2012). The 2010 Mw8.8 Maule, Chile earthquake: Nucleation and rupture propagation controlled by a subducted topographic high. *Geophysical Research Letters*, 39, L19308. <https://doi.org/10.1029/2012GL053184>
- Hippchen, S., & Hyndman, R. D. (2008). Thermal and structural models of the Sumatra subduction zone: Implications for the megathrust seismogenic zone. *Journal of Geophysical Research*, 113, B12103. <https://doi.org/10.1029/2008JB005698>
- Hok, S., Fukuyama, E., & Hashimoto, C. (2011). Dynamic rupture scenarios of anticipated Nankai-Tonankai earthquakes, southwest Japan. *Journal of Geophysical Research*, 116, B12319. <https://doi.org/10.1029/2011JB008492>
- Hong, T.-K., Lee, J., Chi, D., & Park, S. (2017). Seismic velocity changes in the backarc continental crust after the 2011 Mw 9.0 Tohoku-Oki megathrust earthquake. *Geophysical Research Letters*, 44, 10997–11003. <https://doi.org/10.1002/2017gl075447>
- Hong, T.-K., Lee, J., & Hough, S. E. (2015). Long-term evolution of intraplate seismicity in stress shadows after megathrust. *Physics of the Earth and Planetary Interiors*, 245, 59–70. <https://doi.org/10.1016/j.pepi.2015.05.009>
- Hong, T.-K., Lee, J., Kim, W., Hahm, I. K., Woo, N. C., & Park, S. (2017). The 12 September 2016 ML5.8 midcrustal earthquake in the Korean Peninsula and its seismic implications. *Geophysical Research Letters*, 44(7), 3131–3138. <https://doi.org/10.1002/2017gl072899>
- Hong, T.-K., Lee, J., Park, S., & Kim, W. (2018). Time-advanced occurrence of moderate-size earthquakes in a stable intraplate region after a megathrust earthquake and their seismic properties. *Scientific Reports*, 8(1), 1–8. <https://doi.org/10.1038/s41598-018-31600-5>
- Hong, T.-K., Park, S., Lee, J., Chung, D., & Kim, W. (2020). One-off deep crustal earthquake swarm in a stable intracontinental region of the southwestern Korean Peninsula. *Physics of the Earth and Planetary Interiors*, 308, 106582. <https://doi.org/10.1016/j.pepi.2020.106582>
- Ichinose, G. A., Somerville, P., Thio, H. K., Graves, R., & O'Connell, D. (2002). Rupture process of the 1964 Prince William Sound, Alaska, earthquake from the combined inversion of seismic, tsunami, and geodetic data. *Journal of Geophysical Research*, 112, B07306. <https://doi.org/10.1029/2006JB004728>
- Ichinose, G. A., Thio, H. K., Somerville, P. G., Sato, T., & Ishii, T. (2003). Rupture process of the 1944 Tonankai earthquake (Ms 8.1) from the inversion of teleseismic and regional seismograms. *Journal of Geophysical Research*, 108(B10), 2497. <https://doi.org/10.1029/2003JB002393>
- Ide, S. (2013). The proportionality between relative plate velocity and seismicity in subduction zones. *Nature Geoscience*, 6, 780–784. <https://doi.org/10.1038/ngeo1901>
- Ikuta, R., Mitsui, Y., Kurokawa, Y., & Ando, M. (2015). Evaluation of strain accumulation in global subduction zones from seismicity data. *Earth, Planets and Space*, 67(1), 192. <https://doi.org/10.1186/s40623-015-0361-5>
- Ji, C., Wald, D. J., & Helmlinger, D. V. (2002). Source description of the 1999 Hector Mine, California, earthquake, part II: Complexity of slip history. *Bulletin of the Seismological Society of America*, 92(4), 1208–1226. <https://doi.org/10.1785/0120000917>
- Johnson, J. M., & Satake, K. (1999). Asperity distribution of the 1952 great Kamchatka earthquake and its relation to future earthquake potential in Kamchatka. *Pure and Applied Geophysics*, 154, 541–553. https://doi.org/10.1007/978-3-0348-8679-6_8
- Kato, N. (2012). Dependence of earthquake stress drop on critical slip-weakening distance. *Journal of Geophysical Research*, 117, B01301. <https://doi.org/10.1029/2011JB008359>

- Keiding, M., Lund, B., & Árnadóttir, T. (2009). Earthquakes, stress, and strain along an obliquely divergent plate boundary: Reykjanes Peninsula, southwest Iceland. *Journal of Geophysical Research*, *114*, B09306. <https://doi.org/10.1029/2008JB006253>
- King, G. C. P., & Cocco, M. (2001). Fault interaction by elastic stress changes: New clues from earthquake sequences. *Advances in Geophysics*, *44*, I–VIII. [https://doi.org/10.1016/s0065-2687\(00\)80006-0](https://doi.org/10.1016/s0065-2687(00)80006-0)
- King, G. C. P., Stein, R. S., & Lin, J. (1994). Static stress changes and triggering of earthquakes. *Bulletin of the Seismological Society of America*, *84*, 935–953.
- Kirby, S. H., Stein, S., Okal, E. A., & Rubie, D. C. (1996). Metastable mantle phase transformations and deep earthquakes in subducting oceanic lithosphere. *Reviews of Geophysics*, *34*, 261–306. <https://doi.org/10.1029/96rg01050>
- Kobayashi, R., & Koketsu, K. (2005). Source process of the 1923 Kanto earthquake inferred from historical geodetic, teleseismic, and strong motion data. *Earth, Planets and Space*, *57*(4), 261–270. <https://doi.org/10.1186/bf03352562>
- Koerner, A., Kissling, E., & Miller, S. A. (2004). A model of deep crustal fluid flow following the Mw8.0 Antofagasta, Chile, earthquake. *Journal of Geophysical Research*, *109*, B06307. <https://doi.org/10.1029/2003JB002816>
- Konca, A. O., Avouac, J.-P., Sladen, A., Meltzner, A. J., Sieh, K., Fang, P., et al. (2008). Partial rupture of a locked patch of the Sumatra megathrust during the 2007 earthquake sequence. *Nature*, *456*, 631–635. <https://doi.org/10.1038/nature07572>
- Kostoglodov, V., Bandy, W., Dominguez, J., & Mena, M. (1996). Gravity and seismicity over the Guerrero seismic gap, Mexico. *Geophysical Research Letters*, *23*(23), 3385–3388. <https://doi.org/10.1029/96gl03159>
- Kostoglodov, V., Valenzuela, W., Gorbatov, A., Mimiaga, J., Franco, S. I., Alvarado, J. A., & Peláez, R. (2001). Deformation in the Guerrero seismic gap, Mexico, from leveling observation. *Journal of Geodesy*, *75*, 19–32. <https://doi.org/10.1007/s01900000144>
- Koyama, J., Yoshizawa, K., Yomogida, K., & Tsuzuki, M. (2012). Variability of megathrust earthquakes in the world revealed by the 2011 Tohoku-oki Earthquake. *Earth, Planets and Space*, *64*(12), 1189–1198. <https://doi.org/10.5047/eps.2012.04.011>
- Kremer, C., Blewitt, G., & Klein, E. C. (2014). A geodetic plate motion and global strain rate model. *Geochemistry, Geophysics, Geosystems*, *15*(10), 849–853. <https://doi.org/10.1002/2014gc005407>
- Lamb, S. (2005). Shear stresses on megathrusts: Implications for mountain building behind subduction zones. *Journal of Geophysical Research*, *111*, B07401. <https://doi.org/10.1029/2008JB003916>
- Langenbruch, C., & Shapiro, S. A. (2015). Quantitative analysis of rock stress heterogeneity: Implications for the seismogenesis of fluid-injection-induced seismicity. *Geophysics*, *80*(6), WC73–WC88. <https://doi.org/10.1190/geo2015-0061.1>
- Langseth, M. G., & Silver, E. A. (1996). The Nicoya convergent margin: A region of exceptionally low heat flow. *Geophysical Research Letters*, *23*, 891–894. <https://doi.org/10.1029/96gl00733>
- Lay, T., Kanamori, H., Ammon, A. J., Nettler, M., Ward, S. N., Aster, R. C., et al. (2005). The great Sumatra-Andaman earthquake of 26 December 2004. *Science*, *308*(1), 1127–1133. <https://doi.org/10.1126/science.1112250>
- Li, S., & Freymueller, J. T. (2017). Spatial variation of slip behavior beneath the Alaska Peninsula along Alaska-Aleutian subduction zone. *Geophysical Research Letters*, *45*(3), 453–460. <https://doi.org/10.1002/2017GL076761>
- Liberty, L. M., Finn, S. P., Haeussler, P. J., Pratt, T. L., & Peterson, A. (2013). Megathrust splay faults at the focus of the Prince William Sound asperity, Alaska. *Journal of Geophysical Research: Solid Earth*, *118*, 5428–5441. <https://doi.org/10.1002/jgrb.50372>
- Lin, J., & Stein, R. S. (2004). Stress triggering in thrust and subduction earthquakes, and stress interaction between the southern San Andreas and nearby thrust and strike-slip faults. *Journal of Geophysical Research*, *109*, B02303. <https://doi.org/10.1029/2003JB002607>
- Lin, Y. N., Sladen, A., Ortega-Culaciati, F., Simons, M., Avouac, J.-P., Fielding, E. J., et al. (2013). Coseismic and postseismic slip associated with the 2010 Maule Earthquake, Chile: Characterizing the Arauco Peninsula barrier effect. *Journal of Geophysical Research: Solid Earth*, *118*(6), 3142–3159. <https://doi.org/10.1002/jgrb.50207>
- Liu, C., Dong, P., Zhu, B., & Shi, Y. (2018). Stress shadow on the southwest portion of the Longmen Shan Fault impacted the 2008 Wenchuan earthquake rupture. *Journal of Geophysical Research: Solid Earth*, *123*, 9963–9981. <https://doi.org/10.1029/2018jb015633>
- Loveless, J. P., & Meade, B. J. (2010). Geodetic imaging of plate motions, slip rates, and partitioning of deformation in Japan. *Journal of Geophysical Research*, *115*, B02410. <https://doi.org/10.1029/2008JB006248>
- Müller, R. D., Sdrolias, M., Gaina, C., & Roest, W. R. (2008). Age, spreading rates, and spreading asymmetry of the world's ocean crust. *Geochemistry, Geophysics, Geosystems*, *9*(4), Q04006. <https://doi.org/10.1029/2007GC001743>
- Maccafferri, F., Rivalta, E., Passarelli, L., & Jónsson, S. (2013). The stress shadow induced by the 1975–1984 Krafla rifting episode. *Journal of Geophysical Research: Solid Earth*, *118*, 1109–1121. <https://doi.org/10.1002/jgrb.50134>
- MacInnes, B., Kravchunovskaya, E., Pinegina, T., & Bourgeois, J. (2016). Paleotsunamis from the central Kuril Islands segment of the Japan-Kuril-Kamchatka subduction zone. *Quaternary Research*, *86*, 54–66. <https://doi.org/10.1016/j.yqres.2016.03.005>
- Magee, M. E., & Zoback, M. D. (1993). Evidence for a weak interplate thrust fault along the northern Japan subduction zone and implications for the mechanics of thrust faulting and fluid expulsion. *Geology*, *21*, 809–812. [https://doi.org/10.1130/0091-7613\(1993\)021<0809:efawit>2.3.co;2](https://doi.org/10.1130/0091-7613(1993)021<0809:efawit>2.3.co;2)
- Mai, P. M., & Beroza, G. C. (2000). Source scaling properties from finite-fault-rupture models. *Bulletin of the Seismological Society of America*, *90*(3), 604–615. <https://doi.org/10.1785/0119990126>
- Mai, P. M., & Thingbaijam, K. K. S. (2014). SRCMOD: An online database of finite-fault rupture models. *Seismological Research Letters*, *85*(6), 1348–1357. <https://doi.org/10.1785/0220140077>
- Ma, K.-F., Chan, C.-H., & Stein, R. S. (2005). Response of seismicity to Coulomb stress triggers and shadows of the 1999 7.6 Chi-Chi, Taiwan, earthquake. *Journal of Geophysical Research*, *110*, B05S19. <https://doi.org/10.1029/2004JB003389>
- Maunder, B., van Hynen, J., Bouilhol, P., & Magni, V. (2019). Modeling slab temperature: A reevaluation of the thermal parameter. *Geochemistry, Geophysics, Geosystems*, *20*(2), 673–687. <https://doi.org/10.1029/2018gc007641>
- McCloskey, J., Nalbant, S. S., & Steacy, S. (2005). Earthquake risk from co-seismic stress. *Nature*, *434*, 291. <https://doi.org/10.1038/434291a>
- Mendoza, C. (1993). Coseismic slip of two large Mexican earthquakes from teleseismic body waveforms: Implications for asperity interaction in the Michoacan plate boundary segment. *Journal of Geophysical Research*, *98*(B5), 8197–8210. <https://doi.org/10.1029/93jb00021>
- Mendoza, C. (1995). Finite-fault analysis of the 1979 March 14 Petatlan, Mexico, earthquake using teleseismic P waveforms. *Geophysical Journal International*, *121*(3), 675–683. <https://doi.org/10.1111/j.1365-246x.1995.tb06430.x>
- Mendoza, C., & Hartzell, S. (2013). Finite-fault source inversion using teleseismic P waves: Simple parameterization and rapid analysis. *Bulletin of the Seismological Society of America*, *103*(2A), 843–844. <https://doi.org/10.1785/0120120069>
- Mendoza, C., & Hartzell, S. H. (1989). Slip distribution of the 19 September 1985 Michoacan, Mexico, earthquake: Near-source and teleseismic constraints. *Bulletin of the Seismological Society of America*, *79*(3), 655–669. <https://doi.org/10.1785/bssa0790030655>
- Mendoza, C., Hartzell, S., & Monfret, T. (1994). Wide-band analysis of the 3 March 1985 central Chile earthquake: Overall source process and rupture history. *Bulletin of the Seismological Society of America*, *84*(2), 269–283.

- Mignan, A., King, G., Bowman, D., Lacassin, R., & Dmowska, R. (2006). Seismic activity in the Sumatra-java region prior to the December 26, 2004 (Mw9.0-9.3) and March 28, 2005 (Mw8.7) earthquakes. *Earth and Planetary Science Letters*, 244(3-4), 639-654. <https://doi.org/10.1016/j.epsl.2006.01.058>
- Moreno, M., Rosenau, M., & Oncken, O. (2010). 2010 Maule earthquake slip correlates with pre-seismic locking of Andean subduction zone. *Nature*, 467, 198-202. <https://doi.org/10.1038/nature09349>
- Nagai, R., Kikuchi, M., & Yamanaka, Y. (2001). Comparative study on the source processes of recurrent large earthquakes in Sanriku-oki region: The 1968 Tokachi-oki earthquake and the 1994 Sanriku-oki earthquake. *Jishin*, 54(2), 267-280. https://doi.org/10.4294/zisin1948.54.2_267
- Nalbant, S. S., Hubert, A., & King, G. C. P. (1998). Stress coupling between earthquakes in northwest Turkey and the north Aegean Sea. *Journal of Geophysical Research*, 13(24), 24469-24486. <https://doi.org/10.1029/98jb01491>
- Obara, K., & Kato, A. (2016). Connecting slow earthquakes to huge earthquakes. *Science*, 353(6296), 253-257. <https://doi.org/10.1126/science.aaf1512>
- Okazaki, K., & Hirth, G. (2016). Dehydration of lawsonite could directly trigger earthquakes in subducting oceanic crust. *Nature*, 530(7588), 81-84. <https://doi.org/10.1038/nature16501>
- Okuwaki, R., & Yagi, Y. (2002). Rupture process during the Mw 8.1 2017 Chiapas Mexico earthquake: Shallow intraplate normal faulting by slab bending. *Geophysical Journal International*, 150(2), 377-371.
- Oleskevich, D. A., Hyndman, R. D., & Wang, K. (1999). The updip and downdip limits to great subduction earthquakes: Thermal and structural models of Cascadia, south Alaska, SW Japan, and Chile. *Journal of Geophysical Research*, 104(B7), 14965-14991. <https://doi.org/10.1029/1999jb900060>
- Ozawa, S., Nishimura, T., Suito, H., Kobayashi, T., Tobita, M., & Imakiire, T. (2011). Coseismic and postseismic slip of the 2011 magnitude-9 Tohoku-Oki earthquake. *Nature*, 475(7356), 373-376. <https://doi.org/10.1038/nature10227>
- Peacock, S. M., & Wang, K. (1999). Seismic consequences of warm versus cool subduction metamorphism: Examples from southwest and northeast Japan. *Science*, 286, 937-939. <https://doi.org/10.1126/science.286.5441.937>
- Perfettini, H., & Avouac, J.-P. (2004). Stress transfer and strain rate variations during the seismic cycle. *Journal of Geophysical Research*, 109, B06402. <https://doi.org/10.1029/2003JB002917>
- Philibosian, B., Sieh, K., Avouac, J. P., Natawidjaja, D. H., Chiang, H. W., Wu, C.-C., et al. (2017). Earthquake supercycles on the Mentawai segment of the Sunda megathrust in the seventeenth century and earlier. *Journal of Geophysical Research: Solid Earth*, 122(1), 642-676. <https://doi.org/10.1002/2016jb013560>
- Plafker, G. (1965). Tectonic deformation associated with the 1964 Alaska earthquake: The earthquake of 27 March 1964 resulted in observable crustal deformation of unprecedented areal extent. *Science*, 148(3678), 1675-1687. <https://doi.org/10.1126/science.148.3678.1675>
- Pollitz, F. F., Stein, R. S., Sevilgen, V., & Buřgmann, R. (2012). The 11 April 2012 east Indian Ocean earthquake triggered large aftershocks worldwide. *Nature*, 490, 250-253. <https://doi.org/10.1038/nature11504>
- Pulido, N., Nakai, S., Yamanaka, H., Calderon, D., Aguilar, Z., Sekiguchi, T., & Sekiguchi, T. (2014). Estimation of a source model and strong motion simulation for Tacna City, South Peru. *Journal of Disaster Research*, 9(6), 925-930. <https://doi.org/10.20965/jdr.2014.p0925>
- Qiu, Z., & Shi, Y. (2004). Application of observed strain steps to the study of remote earthquake stress triggering. *Acta Seismologica Sinica*, 17, 1-8. <https://doi.org/10.1007/s11589-004-0035-z>
- Ramos, N. T., Dimalanta, C. B., Besana, G. M., Tamayo, R. A., Yumul, G. P., & Maglambayan, V. B. (2005). Seismotectonic reactions to the arc-continent convergence in central Philippines. *Resource Geology*, 55(3), 199-206. <https://doi.org/10.1111/j.1751-3928.2005.tb00241.x>
- Ross, Z. E., Idini, B., Jia, Z., Stephenson, O. L., Zhong, M., Wang, X., et al. (2019). Hierarchical interlocked orthogonal faulting in the 2019 Ridgecrest earthquake sequence. *Science*, 366(6463), 346-351. <https://doi.org/10.1126/science.aaz0109>
- Ruff, L. J. (1989). Do trench sediments affect great earthquake occurrence in subduction zones? *Pure and Applied Geophysics*, 129, 263-282. https://doi.org/10.1007/978-3-0348-9140-0_9
- Rundle, J. B., & Kanamori, H. (1987). Application of an inhomogeneous stress (patch) model to complex subduction zone earthquakes—A discrete interaction matrix approach. *Journal of Geophysical Research*, 92, 2606-2616. <https://doi.org/10.1029/jb092ib03p02606>
- Ryan, H. F., & Scholl, D. W. (1993). Geologic implications of great interplate earthquakes along the Aleutian arc. *Journal of Geophysical Research*, 98(B12), 22135-22146. <https://doi.org/10.1029/93jb02451>
- Saffer, D. M., Silver, E. A., Fisher, A. T., Tobin, H., & Moran, K. (2000). Inferred pore pressures at the Costa Rica subduction zone: Implications for dewatering process. *Earth and Planetary Science Letters*, 177, 193-207. [https://doi.org/10.1016/S0012-821X\(00\)00048-0](https://doi.org/10.1016/S0012-821X(00)00048-0)
- Saffer, D. M., & Wallace, L. M. (2015). The frictional, hydrologic, metamorphic and thermal habitat of shallow slow earthquakes. *Nature Geoscience*, 8, 594-600. <https://doi.org/10.1038/ngeo2490>
- Scholz, C. H. (1990). *The mechanics of earthquakes and faulting* (p. 439). Cambridge University Press.
- Schwartz, S. Y. (1999). Noncharacteristic behavior and complex recurrence of large subduction zone earthquakes. *Journal of Geophysical Research*, 104(23), 111-123. <https://doi.org/10.1029/1999jb900226>
- Schwartz, S. Y., & Rokosky, J. M. (2007). Slow slip events and seismic tremor at circum-pacific subduction zones. *Reviews of Geophysics*, 45, RG3004. <https://doi.org/10.1029/2006RG0020810.1029/2006rg000208>
- Sekiguchi, H., Irikura, K., & Iwata, T. (2002). Source inversion for estimating the continuous slip distribution on a fault—Introduction of Green's functions convolved with a correction function to give moving dislocation effects in subfaults. *Geophysical Journal International*, 150(2), 377-391. <https://doi.org/10.1046/j.1365-246x.2002.01669.x>
- Seno, T. (2017). Subducted sediment thickness and Mw9 earthquakes. *Journal of Geophysical Research: Solid Earth*, 122, 470-491. <https://doi.org/10.1002/2016jb013048>
- Sevilgen, V., Etein, R. S., & Pollitz, F. F. (2012). Stress imparted by the great 2004 Sumatra earthquake shut down transforms and activated rifts up to 400 km away in the Andaman Sea. *Proceedings of the National Academy of Sciences*, 109(38), 15152-15156. <https://doi.org/10.1073/pnas.1208799109>
- Song, S., Beroza, G. C., & Segall, P. (2008). A unified source model for the 1906 San Francisco earthquake. *Bulletin of the Seismological Society of America*, 98(2), 823-831. <https://doi.org/10.1785/0120060402>
- Spinelli, G. A., & Wang, K. (2008). Effects of fluid circulation in subducting crust on Nankai margin seismogenic zone temperatures. *Geology*, 36, 887-890. <https://doi.org/10.1130/g25145a.1>
- Stein, R. S., Barka, A. A., & Dieterich, J. H. (1997). Progressive failure on the north Anatolian fault since 1939 by earthquake stress triggering. *Geophysical Journal International*, 128, 594-604. <https://doi.org/10.1111/j.1365-246x.1997.tb05321.x>
- Stein, R. S., King, G. C. P., & Lin, J. (1994). Stress triggering of the 1994 Mw6.7 Northridge, California, earthquake by its predecessors. *Science*, 265, 1432-1435. <https://doi.org/10.1126/science.265.5177.1432>

- Strasser, F. O., Arango, M. C., & Bommer, J. J. (2010). Scaling of the source dimensions of interface and intraslab subduction-zone earthquakes with moment magnitude. *Seismological Research Letters*, 81(6), 941–950. <https://doi.org/10.1785/gssrl.81.6.941>
- Streit, J. E., & Cox, S. F. (2001). Fluid pressures at hypocenters of moderate to large earthquakes. *Journal of Geophysical Research*, 106(B2), 2235–2243. <https://doi.org/10.1029/2000jb900359>
- Suwa, Y., Miura, S., Hasegawa, A., Sato, T., & Tachibana, K. (2006). Interplate coupling beneath NE Japan inferred from three-dimensional displacement field. *Journal of Geophysical Research*, 111, B04402. <https://doi.org/10.1029/2004JB003203>
- Syracuse, E. M., van Keken, P. E., & Abers, G. A. (2010). The global range of subduction zone thermal models. *Physics of the Earth and Planetary Interiors*, 183(1–2), 73–90. <https://doi.org/10.1016/j.pepi.2010.02.004>
- ten Brink, U., & Lin, J. (2004). Stress interaction between subduction earthquakes and forearc strike-slip faults: Modeling and application to the northern Caribbean plate boundary. *Journal of Geophysical Research*, 109, B12310. <https://doi.org/10.1029/2004JB003031>
- Thatcher, W. (1990). Order and diversity in the modes of Circum-Pacific earthquake recurrence. *Journal of Geophysical Research*, 96(B3), 2609–2623. <https://doi.org/10.1029/jb095ib03p02609>
- Toda, S., Stein, R. S., Beroza, G. C., & Marsan, D. (2012). Aftershocks halted by static stress shadows. *Nature Geoscience*, 5, 410–413. <https://doi.org/10.1038/ngeo1465>
- Toda, S., Stein, R. S., Reasenber, P. A., Dieterich, J. H., & Yoshida, A. (1998). Stress transferred by the 1995 Mw= 6.9 Kobe, Japan, shock: Effect on aftershocks and future earthquake probabilities. *Journal of Geophysical Research*, 103(B10), 24543–24565. <https://doi.org/10.1029/98jb00765>
- Toda, S., Stein, R. S., Richards-Dinger, K., & Bozkurt, S. (2005). Forecasting the evolution of seismicity in southern California: Animations built on earthquake stress transfer. *Journal of Geophysical Research*, 110(B5), B05S16. <https://doi.org/10.1029/2004JB003415>
- Townend, J., & Zoback, M. D. (2006). Stress, strain, and mountain building in central Japan. *Journal of Geophysical Research*, 111, B03411. <https://doi.org/10.1029/2005JB003759>
- Uchida, N., Iinuma, T., Nadeau, R. M., Bürgmann, R., & Hino, R. (2016). Periodic slow slip triggers megathrust zone earthquakes in north-eastern Japan. *Science*, 351(6272), 488–492. <https://doi.org/10.1126/science.aad3108>
- Uyeda, S., & Kanamori, H. (1979). Back-arc opening and the mode of subduction. *Journal of Geophysical Research*, 84(1), 061. <https://doi.org/10.1029/jb084ib03p01049>
- Villegas-Lanza, J. C., Chlieh, M., Cavalié, O., Tavera, H., Baby, P., Chire-Chira, J., & Nocquet, J.-M. (2016). Active tectonics of Peru: Heterogeneous interseismic coupling along the Nazca megathrust, rigid motion of the Peruvian Sliver, and Subandean shortening accommodation. *Journal of Geophysical Research: Solid Earth*, 121(7), 7371–7394. <https://doi.org/10.1002/2016jb013080>
- vonHerzen, R., Ruppel, C., Molnar, P., Nettles, M., Nagihara, S., & Ekstrom, G. (2001). A constraint on the shear stress at the Pacific-Australian plate boundary from heat flow and seismicity at the Kermadec forearc. *Journal of Geophysical Research*, 106(B4), 6817–6883. <https://doi.org/10.1029/2000jb900469>
- Wada, I., & Wang, K. (2009). Common depth of slab-mantle decoupling: Reconciling diversity and uniformity of subduction zones. *Geochemistry, Geophysics, Geosystems*, 10, 10009. <https://doi.org/10.1029/2009GC002570>
- Wada, I., Wang, K., He, J., & Hyndman, R. D. (2008). Weakening of the subduction interface and its effects on surface heat flow, slab dehydration, and mantle wedge serpentinization. *Journal of Geophysical Research*, 113, B04402. <https://doi.org/10.1029/2007JB005190>
- Wald, D. J., & Heaton, T. H. (1994). Spatial and temporal distribution of slip for the 1992 Landers, California, earthquake. *Bulletin of the Seismological Society of America*, 84(3), 668–691.
- Wallace, L. M., Webb, S. C., Ito, Y., Mochizuki, K., Hino, R., Henrys, S., et al. (2016). Slow slip near the trench at the Hikurangi subduction zone, New Zealand. *Science*, 352(6286), 701–704. <https://doi.org/10.1126/science.aaf2349>
- Wang, K., & He, J. (1999). Mechanics of low-stress forearcs: Nankai and Cascadia. *Journal of Geophysical Research*, 104(B7), 15191–15205. <https://doi.org/10.1029/1999jb900103>
- Wang, K., Mulder, T., Rogers, G. C., & Hyndman, R. D. (1995). Case for very low coupling stress on the Cascadia subduction fault. *Journal of Geophysical Research*, 100, 12907–12918. <https://doi.org/10.1029/95jb00516>
- Wang, K., & Suyehiro, K. (1999). How does plate coupling affect crustal stresses in Northeast and Southwest Japan? *Geophysical Research Letters*, 26(15), 2307–2310. <https://doi.org/10.1029/1999gl900528>
- Wang, W.-H. (2000). Static stress transfer and aftershock triggering by the 1999 Chi-Chi earthquake in Taiwan. *Terrestrial, Atmospheric and Oceanic Sciences*, 11, 631–624. [https://doi.org/10.3319/tao.2000.11.3.631\(cce\)](https://doi.org/10.3319/tao.2000.11.3.631(cce))
- Wei, M., McGuire, J. J., & Richardson, E. (2012). A slow slip event in the south central Alaska Subduction Zone and related seismicity anomaly. *Geophysical Research Letters*, 39, L15309. <https://doi.org/10.1029/2012GL052351>
- Wells, D. L., & Coppersmith, K. J. (1994). New empirical relationships among magnitude, rupture length, rupture width, rupture area, and surface displacement. *Bulletin of the Seismological Society of America*, 84, 974–1002.
- Wells, R. E., Blakely, R. J., Sugiyama, Y., Scholl, D. W., & Dinterman, P. A. (2003). Basin-centered asperities in great subduction zone earthquakes: A link between slip, subsidence, and subduction erosion? *Journal of Geophysical Research*, 108(B10), 2507. <https://doi.org/10.1029/2002JB002072>
- Widiyantoro, S., Gunawan, E., Muhari, A., Rawlinson, N., Mori, J., Hanifa, N. R., et al. (2020). Implications for megathrust earthquakes and tsunamis from seismic gaps south of Java Indonesia. *Scientific Reports*, 10(1), 1–11. <https://doi.org/10.1038/s41598-020-72142-z>
- Williams, C. F., Grubb, F. V., & Galanis, S. P., Jr. (2004). Heat flow in the SAFOD pilot hole and implications for the strength of the San Andreas Fault. *Geophysical Research Letters*, 31, L15S14. <https://doi.org/10.1029/2003GL019352>
- Wyss, M., & Wiemer, S. (1999). How can one test the seismic gap hypothesis? The case of repeated ruptures in the Aleutians. *Pure and Applied Geophysics*, 155, 259–278. <https://doi.org/10.1007/s000240050265>
- Yagi, Y. (2004). Source rupture process of the 2003 Tokachi-oki earthquake determined by joint inversion of teleseismic body wave and strong ground motion data. *Earth, Planets and Space*, 56, 311–316. <https://doi.org/10.1186/bf03353057>
- Yagi, Y., & Fukahata, Y. (2011). Rupture process of the 2011 Tohoku-oki earthquake and absolute elastic strain release. *Geophysical Research Letters*, 38(19), L19307. <https://doi.org/10.1029/2011GL048701>
- Yagi, Y., Kikuchi, M., Yoshida, S., & Yamanaka, Y. (1998). Source process of the Hyuga-nada earthquake of April 1, 1968 (Mjma 7.5), and its relationship to the subsequent seismicity. *Jishin*, 51(1), 139–148. https://doi.org/10.4294/zisin.1948.51.1_139
- Yamanaka, Y., & Kikuchi, M. (2004). Asperity map along the subduction zone in northeastern Japan inferred from regional seismic data. *Journal of Geophysical Research*, 109(B7), B07307. <https://doi.org/10.1029/2003JB002683>
- Yamazaki, F., Zavala, C., Nakai, S., Koshimura, S., Saito, T., Midorikawa, S., et al. (2014). Summary report of the SATREPS project on earthquake and tsunami disaster mitigation technology in Peru. *Journal of Disaster Research*, 9(6), 925–930. <https://doi.org/10.20965/jdr.2014.p0915>
- Ye, L., Kanamori, H., & Lay, T. (2018). Global variations of large megathrust earthquake rupture characteristics. *Science Advances*, 4(3), eaao4915. <https://doi.org/10.1126/sciadv.aao4915>

- Ye, L., Lay, T., Kanamori, H., & Koper, K. D. (2013). Energy release of the 2013 Mw 8.3 Sea of Okhotsk earthquake and deep slab stress heterogeneity. *Science*, *341*(6152), 1380–1384. <https://doi.org/10.1126/science.1242032>
- Yokota, Y., Ishikawa, T., Watanabe, S., Tashiro, T., & Asada, A. (2016). Seafloor geodetic constraints on interplate coupling of the Nankai Trough megathrust zone. *Nature*, *534*, 374–377. <https://doi.org/10.1038/nature17632>
- Zoback, M. L. (1992). First-and second-order patterns of stress in the lithosphere: The World Stress Map Project. *Journal of Geophysical Research*, *97*(B8), 11703–11728. <https://doi.org/10.1029/92jb00132>